A Decomposition of Feedback Contributions to Polar Warming Amplification

PATRICK C. TAYLOR

NASA Langley Research Center, Hampton, Virginia

MING CAI

Department of Earth, Ocean and Atmospheric Science, The Florida State University, Tallahassee, Florida

AIXUE HU, JERRY MEEHL, AND WARREN WASHINGTON

Climate Change Research, Climate and Global Dynamics, National Center for Atmospheric Research, Boulder, Colorado*

GUANG J. ZHANG

Scripps Institution of Oceanography, University of California, San Diego, San Diego, California

(Manuscript received 14 September 2012, in final form 7 March 2013)

ABSTRACT

Polar surface temperatures are expected to warm 2–3 times faster than the global-mean surface temperature: a phenomenon referred to as polar warming amplification. Therefore, understanding the individual process contributions to the polar warming is critical to understanding global climate sensitivity. The Coupled Feedback Response Analysis Method (CFRAM) is applied to decompose the annual- and zonal-mean vertical temperature response within a transient 1% yr^{-1} CO_2 increase simulation of the NCAR Community Climate System Model, version 4 (CCSM4), into individual radiative and nonradiative climate feedback process contributions. The total transient annual-mean polar warming amplification (amplification factor) at the time of CO_2 doubling is +2.12 (2.3) and +0.94 K (1.6) in the Northern and Southern Hemisphere, respectively. Surface albedo feedback is the largest contributor to the annual-mean polar warming amplification accounting for +1.82 and +1.04 K in the Northern and Southern Hemisphere, respectively. Net cloud feedback is found to be the second largest contributor to polar warming amplification (about +0.38 K in both hemispheres) and is driven by the enhanced downward longwave radiation to the surface resulting from increases in low polar water cloud. The external forcing and atmospheric dynamic transport also contribute positively to polar warming amplification: +0.29 and +0.32 K, respectively. Water vapor feedback contributes negatively to polar warming amplification because its induced surface warming is stronger in low latitudes. Ocean heat transport storage and surface turbulent flux feedbacks also contribute negatively to polar warming amplification. Ocean heat transport and storage terms play an important role in reducing the warming over the Southern Ocean and Northern Atlantic Ocean.

1. Introduction

Enhanced warming of the polar surface temperature with respect to the global-mean temperature, referred to as polar warming amplification (PWA), has been a robust feature of externally forced climate model simulations for more than 30 years (e.g., Manabe and Wetherald 1975; Manabe and Stouffer 1980; Hansen et al. 1984; Rind 1987; Lu and Cai 2010; Cai and Tung 2012) and is considered an inherent characteristic of the climate system. Modern general circulation models (GCMs) from phase 3 of the Coupled Model Intercomparison Project (CMIP3) have indicated that polar regions are likely to warm at least twice as much as the global average (Meehl et al. 2007). PWA is further supported by observations, which indicate that the Arctic likely (66%–90% confidence)

*The National Center for Atmospheric Research is sponsored by the National Science Foundation.

Corresponding author address: Ming Cai, Department of Earth, Ocean, and Atmospheric Science, The Florida State University, 1017 Academic Way, Tallahassee, FL 32306.
E-mail: mcai@fsu.edu

DOI: 10.1175/JCLI-D-12-00696.1

warmed over the last 50 years (ACIA 2005) and has outpaced global-mean warming by 2–3 times from 1970 to 2008 (Chylek et al. 2009). Despite the robustness of PWA predictions amongst CMIP3 models, the largest intermodel spread in regional warming magnitudes is found in polar regions (Bony et al. 2006; Meehl et al. 2007). In addition, the magnitude of polar warming is an important constraint on sea and land ice melt projections, sea level rise, and global climate sensitivity.

The polar regions, specifically the Arctic, are the most climatically sensitive areas of the globe (e.g., Solomon et al. 2007). The enhanced sensitivity of high-latitude regions to an external forcing is linked to several radiative and nonradiative feedback processes (Rind et al. 1995; Holland and Bitz 2003; Hall 2004; Cai 2005, 2006; Cai and Lu 2007; Winton 2006; Lu and Cai 2010; Hwang et al. 2011; Alexeev and Jackson 2013). The surface albedo feedback is cited as the most significant contributor to PWA (e.g., Manabe and Wetherald 1975; Hall 2004; Winton 2006; Serreze and Barry 2011). Studies suggest that the surface albedo feedback accounts for nearly half of the polar surface temperature increase under a CO_2 forcing (Hall 2004). However, Winton (2006) concludes, using a top-of-atmosphere (TOA) perspective, that the surface albedo feedback may not be the most important contributor to PWA but rather combined longwave (LW) feedbacks. Idealized climate simulations demonstrate that PWA can occur in the absence of the surface albedo feedback (Cai 2005, 2006; Cai and Lu 2007; Graversen and Wang 2009; Lu and Cai 2010; Langen et al. 2012; Cai and Tung 2012). Graversen and Wang (2009) show that PWA is only increased by 15% when the surface albedo feedback is active. Ocean heat transport also influences PWA through either a direct deposition of energy at the polar surface (Holland and Bitz 2003) or a cooling of the polar surface through energy storage and transport to the deep ocean (Bitz et al. 2012), respectively. Atmospheric heat transports are also critical to PWA. Cai (2005) attributes ~25% of the total 3.2-K high-latitude warming to enhanced atmospheric transport in an idealized climate model. Langen et al. (2012) confirm the importance of atmospheric transport to PWA in GCM aquaplanet simulations. Moreover, Lu and Cai (2010) and Cai and Tung (2012) demonstrate that poleward dry static energy transport is sufficient to produce PWA on its own, in the absence of surface albedo, surface evaporation, and latent heat transport feedbacks.

Recently, more attention has been paid to the importance of clouds to PWA (e.g., Vavrus 2004; Holland and Bitz 2003) and interannual sea ice variability (e.g., Kay and Gettelman 2009). Holland and Bitz (2003) show that cloud feedbacks contribute to the intermodel spread in PWA, indicating a positive correlation between increased cloud cover and simulated PWA in GCMs. Vavrus (2004) suggests that Arctic cloud feedbacks account for up to 40% of total Arctic warming under increased CO_2. The cloud influence on PWA inferred from the TOA radiative feedback perspective is contradictory to the results from a surface energy budget perspective. TOA net cloud feedback in CMIP3 models tends to be positive in the tropics and negative in high latitudes (Soden et al. 2008; Taylor et al. 2011a; Zelinka and Hartmann 2012), suggesting that clouds oppose PWA. Lu and Cai (2009b) indicate significant contributions to polar surface warming by clouds, particularly during polar night, due to a cloud-induced enhancement of downward longwave radiation to the surface. Idealized modeling studies of PWA are generally insufficient to investigate the influence of clouds (e.g., Cai 2005; Lu and Cai 2010; Langen et al. 2012). A main objective of this study is to explain the differences between PWA feedback contributions from the TOA and surface perspectives by decomposing the individual feedback process contributions to the vertically resolved atmosphere and surface polar temperature response in a coupled atmosphere–ocean GCM.

This study quantifies the contributions of various physical processes to the global temperature response and PWA in a coupled atmosphere ocean GCM forced with increased CO_2. The Coupled Feedback Response Analysis Method (CFRAM; Lu and Cai 2009a; Cai and Lu 2009, hereafter LC09 and CL09, respectively) is employed to directly attribute polar atmospheric and surface temperature changes to individual physical processes thereby quantifying the role individual feedbacks play in PWA. A transient simulation forced by 1% yr^{-1} CO_2 increase until doubling and the corresponding 1850 control simulation with a constant CO_2 concentration from the National Center for Atmospheric Research (NCAR) Community Climate System Model, version 4 (CCSM4), are used. The model characteristics and simulation specifics are discussed in section 2. Details of CFRAM are given in section 3, and section 4 presents the attribution results. A discussion of the individual process contributions to PWA is provided in section 5. Section 6 provides a summary and conclusion.

2. Model simulation and response

The NCAR CCSM4 is a coupled atmosphere–ocean GCM. The atmospheric component of CCSM4 is the Community Atmospheric Model, version 4 (CAM4), with a finite volume dynamic core, 1° horizontal resolution, and 26 vertical levels. The ocean model is the Parallel Ocean Program, version 2 (POP2), with 1° horizontal resolution enhanced to 0.27° in the equatorial region and

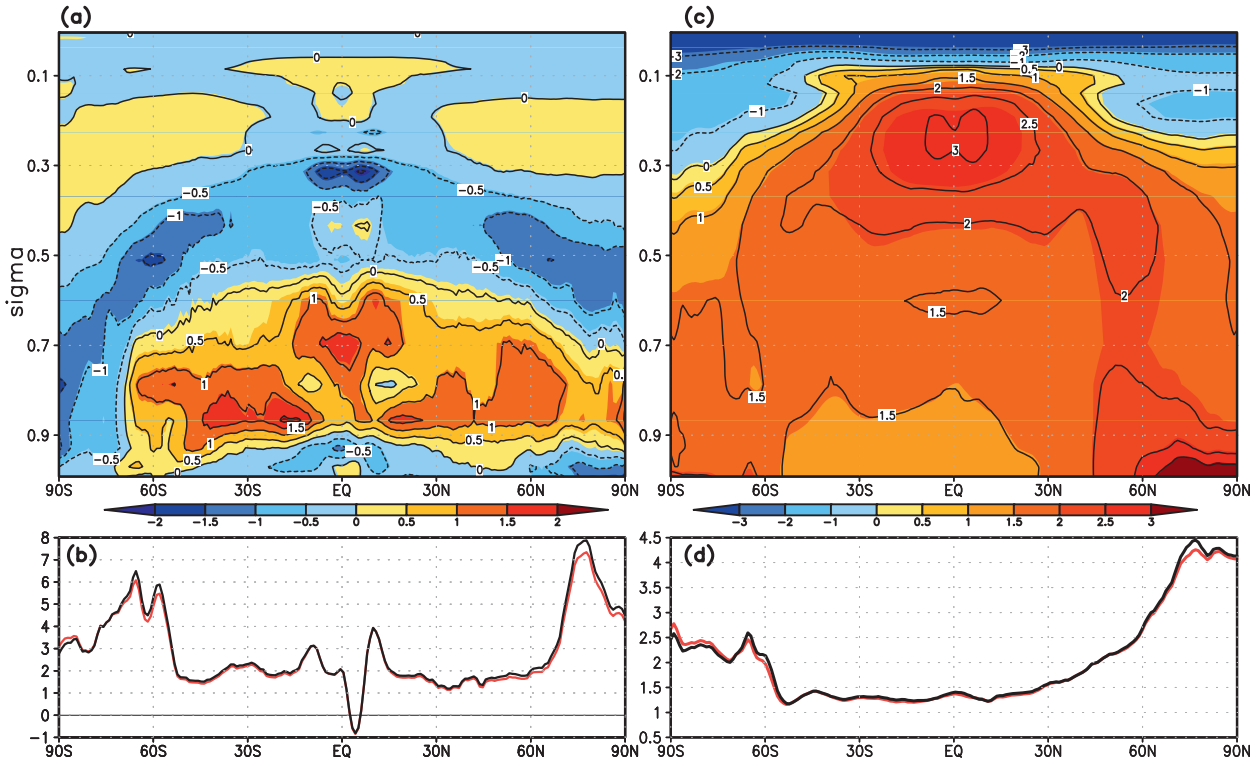

FIG. 1. Zonal mean of changes in the total radiative energy flux convergence $\Delta(S - R)$ (positive values indicate convergence, W m^{-2}) (a) in the atmosphere (shading) and (b) at the surface (red line) and the zonal mean of (c) air (shading) and (d) surface (red line) temperature response (K) of NCAR CCSM4 global warming simulations. Contours in (a) and the black line in (b) correspond to the sum of the partial radiation perturbations due to the external forcing (ΔF^{ext}), water vapor feedback [$\Delta^{\text{WV}}(S - R)$], cloud feedback [$\Delta^{c}(S - R)$], surface albedo feedback ($\Delta^{\text{alb}}S$), and change in temperature [$-(\partial R/\partial T)\Delta T$]. Contours in (c) and the black line in (d) correspond to the sum of partial temperature changes based on CFRAM analysis, equaling the sum of their counterparts in (c) and (d) in Figs. 2–3 and 7–9 and in (b),(d),(f), and (h) in Fig. 10 (note that the atmospheric portions are not shown in Fig. 10).

60 levels vertically. Please see Gent et al. (2011) for more CCSM4 details.

Two model simulations are analyzed: 1) preindustrial control simulation and 2) 1% yr^{-1} compound CO_2 increase. In the preindustrial control simulation, all forcings are constant at year 1850 levels where the CO_2 concentration is 284.7 ppm. The annual-mean climatology is taken as the 20-yr average of the control climate simulation between 1920 and 1940. The second simulation is forced with a transient 1% yr^{-1} compound CO_2 increase. The annual-mean climatology of the transient climate simulation is defined as the 20-yr average centered on the time of CO_2 doubling from preindustrial levels. The transient climate response to the CO_2 forcing is then given as the difference between the transient and control climatology. The global-mean surface temperature change in the transient climate response is 1.64 K, slightly higher than CCSM3 and roughly half the equilibrium warming (Bitz et al. 2012).

The salient features of the CCSM4 zonal annual-mean atmospheric (Fig. 1a) and surface (Fig. 1b) temperature response are (i) stratospheric cooling, (ii) a maximum warming center in upper troposphere in the tropics, (iii) a stronger surface warming in the polar area than in the tropics. The combination of (ii) and (iii) also indicates (iv) a decrease in the vertical temperature gradient in the tropics but an increase in the vertical temperature gradient in high latitudes and (v) a decrease in the meridional temperature gradient at the surface and lower troposphere but an increase in the meridional temperature gradient in the upper troposphere. In addition to the stronger surface warming in high latitudes than in low latitudes (Fig. 1a), the surface warming over land is also larger than over the oceans (not shown).

The overall cloud representation in CAM4 on the global scale is similar to observations. Kay et al. (2012) demonstrate that the root-mean-square errors of the CAM4 global annual-mean TOA shortwave (SW) and longwave cloud forcing is only ~1 W m^{-2} in comparison with Clouds and Earth's Radiant Energy System (CERES; Loeb et al. 2009) observations. Regionally, although the simulated cloud fraction matches the satellite

observations broadly, CAM4 underestimates the global annual-mean cloud fraction and produces large biases in certain regions (Gettelman et al. 2012; Kay et al. 2012; Medeiros et al. 2012; Barton et al. 2012). In the Arctic, the simulated cloud properties agree reasonably well with observations (Kay et al. 2012; Barton et al. 2012). It should be noted that polar cloud observations have significant uncertainties.

3. Coupled feedback response analysis method

The CFRAM technique (LC09; CL09), formulated for quantifying contributions to the 3D global warming pattern, is applied to the transient CCSM4 climate response. CFRAM is based on the energy balance equation of the coupled atmosphere–surface system, similar to the partial radiative perturbation (Wetherald and Manabe 1988) and the radiative kernel method (Soden and Held 2006). CFRAM goes beyond traditional feedback diagnostic methods by 1) measuring feedback strengths in units of temperature and 2) considering the entire atmospheric column and surface temperature response. This analysis is particularly useful when there is a decoupling between the TOA and surface radiative response. Moreover, CFRAM considers both radiative and nonradiative feedback processes explicitly, whereas the TOA-based feedback analysis can only consider radiative feedback processes with nonradiative feedback processes hidden in part of the lapse rate feedback (LC09; CL09). The CFRAM equation is derived from the surface-column energy balance equation (LC09; CL09) and is given by

$$\Delta\mathbf{T} = \left(\frac{\mathbf{R}}{\mathbf{T}}\right)^{-1}[\Delta\mathbf{F}^{\text{ext}} + \Delta^{\text{WV}}(\mathbf{S}-\mathbf{R}) + \Delta^{c}(\mathbf{S}-\mathbf{R}) + \Delta^{\text{alb}}\mathbf{S} + \Delta\mathbf{Q}^{\text{atmos\_dyn+storage}} + \Delta\mathbf{Q}^{\text{ocn\_dyn+storage}} + \Delta\mathbf{Q}^{\text{LH}} + \Delta\mathbf{Q}^{\text{SH}} - \Delta^{\text{Err}}(\mathbf{S}-\mathbf{R})]. \quad (1)$$

The vector **S** is the vertical profile of the solar radiation absorbed by atmospheric layers and the surface layer, whereas **R** corresponds to the vertical profile of the net longwave radiation emitted by atmospheric layers and the surface layer. Each term inside the square brackets represents the vertical profile of an energy flux convergence perturbation in each of the atmospheric layers and the surface layer in units of watts per square meter. Specifically, $\Delta\mathbf{F}^{\text{ext}}$ is the vertical profile of the change in radiative energy flux convergence at each atmospheric layer and at the surface layer due to CO_2 forcing alone; $\Delta^{\text{wv}}(\mathbf{S}-\mathbf{R})$ and $\Delta^{c}(\mathbf{S}-\mathbf{R})$ correspond to the vertical profiles of changes in radiative flux convergence due to changes in atmospheric water vapor and cloud properties, respectively; $\Delta^{\text{alb}}\mathbf{S}$ is the vertical profile of changes in solar energy absorbed by the atmospheric and surface layer due to changes in surface albedo; $\Delta\mathbf{Q}^{\text{atmos\_dyn+storage}}$ is the change in the vertical profile of energy convergence into an atmospheric layer due to (i) convective/large-scale vertical transport of energy into the layer from other layers in the same column and (ii) horizontal transport of energy into the layer of the column from its neighbor columns at the same layer and the atmospheric energy storage; $\Delta\mathbf{Q}^{\text{ocn\_dyn+storage}}$ is the change in the energy convergence and storage at the surface; and $\Delta\mathbf{Q}^{\text{LH}}$ and $\Delta\mathbf{Q}^{\text{SH}}$ are zero in all layers except at the surface layer and the layer above. At the surface, $\Delta Q^{\text{LH}} = -\Delta(\text{LH})$ and $\Delta Q^{\text{SH}} = -\Delta(\text{SH})$, where LH and SH denote surface turbulent latent and sensible heat fluxes, respectively, following the traditional sign convention, namely that positive values mean upward energy flux leaving from the surface to the atmosphere. In the lowest atmosphere layer above surface, $\Delta Q^{\text{LH}} = \Delta(\text{LH})$ and $\Delta Q^{\text{SH}} = \Delta(\text{SH})$, representing the changes in energy convergence into the lowest-atmospheric layer from the surface due to surface turbulent latent and sensible heat fluxes, respectively. The term $\Delta^{\text{Err}}(\mathbf{S}-\mathbf{R})$ is the error in the offline radiative transfer calculation (to be discussed further below); $(\partial\mathbf{R}/\partial\mathbf{T})\Delta\mathbf{T}$ corresponds approximately to the change in the vertical profile of divergent radiative energy flux due to the atmospheric and surface temperature response. The $(\partial\mathbf{R}/\partial\mathbf{T})$ matrix is called the Planck feedback matrix whose *j*th column represents the vertical profile of the change in the divergence of radiative energy fluxes due to a 1-K warming at the *j*th layer alone. Readers may consult Fig. 1 of LC09 for an illustration of $(\partial\mathbf{R}/\partial\mathbf{T})$.

The Fu–Liou radiative transfer model (Fu and Liou 1992, 1993) is used to compute radiative heating rate perturbations at each longitude–latitude grid point. Perturbation calculations for each radiative feedback are performed following Wetherald and Manabe (1988), except the entire column radiative heating rate profiles are archived. Clouds are handled in this study using a variation of the Monte Carlo Independent Column Approximation (MCICA; Pincus et al. 2003) used previously by Taylor et al. (2011a,b) to diagnose cloud feedback. MCICA is performed by subdividing each model grid box into 100 subcolumns and then generating cloud profiles for each. The subcolumn cloud profiles are generated using a maximum random overlap cloud generator (Räisänen et al. 2004) based on the annual-mean climatological cloud properties (cloud fraction, liquid, and ice cloud mixing ratios) derived from the CCSM4 simulations. Calculating each radiative term in

(1) overall grids results in a series of 3D radiative energy flux perturbations. The vertical summation of each radiative heating rate perturbation in (1) in units of W m^{-2} from the surface to the top layer is the net downward radiative energy flux perturbation at TOA due to that term and is identical to their counterparts obtained by applying the partial radiative perturbation (PRP) method (Wetherald and Manabe 1988) or radiative kernel methods (Soden and Held 2006; Soden et al. 2008). Likewise, the vertical summation of $\Delta\mathbf{F}^{\text{ext}}$ from the surface to the tropopause corresponds to the radiative forcing at the tropopause without stratospheric adjustment as conventionally defined (e.g., Hansen et al. 1997). Vertical summation of $(\partial\mathbf{R}/\partial\mathbf{T})\Delta\mathbf{T}$ from the surface to TOA corresponds to the combined Planck and lapse rate feedbacks from the PRP and radiative kernel methods.

Standard CCSM4 outputs include 3D solar heating and longwave cooling rates in the atmosphere and all radiative energy fluxes at the surface. The solar heating and longwave cooling rates are converted from kelvins per day to watts per square meter in each atmospheric layer by multiplying the climatological mean heating/cooling rates in kelvins per day with a factor of 86 400/$(c_p\delta m)$, where c_p is the heat capacity of air at a constant pressure and δm is the climatological mean mass of the atmospheric layer under consideration. These outputs enable us to directly quantify the errors in the offline calculations defined as

$$\Delta^{\text{Err}}(\mathbf{S}-\mathbf{R}) = \Delta(\mathbf{S}-\mathbf{R}) - \Delta(\mathbf{S}^{\text{CCSM4}} - \mathbf{R}^{\text{CCSM4}}), \quad (2)$$

where superscript CCSM4 indicates the results derived directly from CCSM4 output, and the terms without the superscript are derived from the offline calculation. Note that the errors calculated from (2) are not due to the linearization of the radiative transfer model but are from (i) differences between the radiation models used, (ii) using the time mean versus instantaneous fields as inputs for our offline radiation calculations, and (iii) the conversion from kelvins per day to watts per square meter, which should be done before taking any time mean since δm is time dependent. Therefore, the conversion taken after the time mean also introduces some error in inferring the dynamical heating field in the atmosphere from the mean CCSM4 solar heating and longwave cooling rate output, although it should be smaller than the errors due to (i) and (ii).

Nonradiative energy fluxes are taken from the CCSM4 output. The nonradiative energy fluxes included in the standard CCSM4 output are associated with atmospheric turbulent motions within the boundary layer [i.e., surface turbulent sensible (SH) and latent heat (LH) fluxes]. Nonradiative fluxes associated with convective and large-scale advective energy transport are not standard output. Therefore, $\Delta\mathbf{Q}^{\text{atmos\_dyn+storage}}$ is inferred using 3D solar heating and longwave cooling rate in each atmospheric layer as

$$\begin{aligned}\Delta\mathbf{Q}^{\text{atmos\_dyn+storage}} &= \Delta\mathbf{Q}^{\text{atmos\_dyn}} - \Delta\left(\frac{\partial\mathbf{E}}{\partial t}\right)\\ &= -\Delta(\mathbf{S}^{\text{CCSM4}} - \mathbf{R}^{\text{CCSM4}}), \quad (3)\end{aligned}$$

where $\Delta\mathbf{Q}^{\text{atmos\_dyn+storage}}$ is the vertical profile at the grid point under consideration. Similarly, the surface net downward solar and longwave radiation fluxes, LH and SH, from CCSM4 standard output are used to infer the net convergence of nonradiative energy fluxes by the ocean circulation and the ocean heat storage term as

$$\begin{aligned}\Delta Q^{\text{ocn\_dyn+storage}} &= \Delta Q^{\text{ocn\_dyn}} - \Delta\left(\frac{E_{\text{ocean}}}{t}\right)\\ &= -\Delta\left(S_{\text{surf}}^{\text{CCSM4}} - R_{\text{surf}}^{\text{CCSM4}}\right)\\ &\quad + \Delta\text{LH} + \Delta\text{SH}. \quad (4)\end{aligned}$$

The value of $\Delta Q^{\text{ocn\_dyn+storage}}$ is zero, except at the surface equaling the lhs of (4). As a result of the errors in the offline calculation (section 4e), $\Delta Q^{\text{atmos\_dyn+storage}}$ and $\Delta Q^{\text{ocn\_dyn+storage}}$ are determined from changes in the net radiative cooling/heating rate outputs from the CCSM4 output.

As in PRP and radiative kernel feedback diagnostic methods, one of the two main assumptions in CFRAM is that the total radiative energy flux perturbations can be linearly decomposed to the sum of the partial radiative energy flux perturbations by omitting higher order terms. The other main assumption is that the radiative energy flux perturbations can be calculated in offline mode from time-mean fields using a different radiative transfer model. To the best of our knowledge, a direct validation has not been done in the literature. Here the linearization approximation is validated at each grid point and in each vertical layer; the PRP and radiative kernel methods only require the linearization to be valid at TOA or tropopause level. The shading in Fig. 1c and the red curve in Fig. 1d correspond to the zonal mean of the sum of all radiative perturbation terms in the atmosphere and at the surface, whereas the black contour lines and black curve represent the total perturbation computed offline. The fact that the color and line contours in Fig. 1c and the two curves in Fig. 1d overlap nearly exactly indicates that the total radiative energy perturbations in response to the doubling of CO_2 can be calculated using the linearization method.

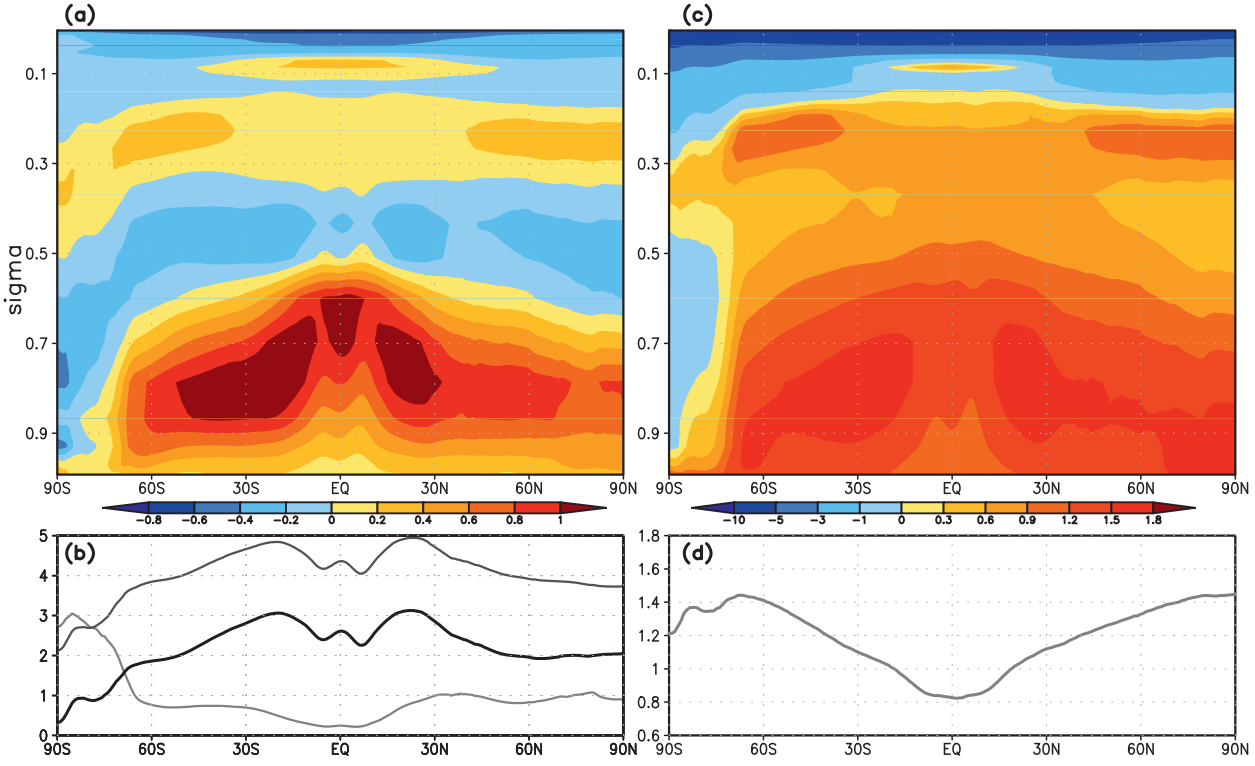

FIG. 2. Zonal mean of perturbations of radiative energy flux convergence ($\mathrm{W\,m^{-2}}$) due to external forcing (ΔF^{ext}) in (a) the atmosphere and (b) at the surface (red line) in units of and zonal mean of partial air temperature changes ΔT^{ext} (K) due to ΔF^{ext} alone in (c) atmosphere and (d) at the surface. The blue and black curves in (b) correspond to the net downward radiation energy flux perturbation due to the external forcing at the tropopause ($\sigma = 0.266$) and the TOA, respectively.

Linearization errors in atmospheric column radiative heating rates are small, as the case at the TOA reported in previous studies (Soden and Held 2006; Soden et al. 2008).

The linear decomposition is then applied to obtain the partial temperature changes due to each term on the rhs of (1). Solving (1) grid point by grid point enables us to obtain 3D profiles of these partial temperature changes. For an easy reference, partial temperature changes are denoted as ΔT^{x} with the superscript x representing one of the eight superscripts or "Err" from (1). Comparing the sum of individual partial temperature changes verifies the accuracy of the CFRAM decomposition (contour lines in Fig. 1a and the black curve in Fig. 1b) with the total temperature change derived from the CCSM4 climate simulations (shading in Fig. 1a and red curve in Fig. 1b). It is shown that the contours nearly coincide with the shading in the troposphere, although there exist some noticeable differences in the stratosphere. This confirms that these partial temperature changes due to the external forcing and feedbacks are indeed addable to the total temperature change obtained from the model simulation.

4. Attribution of the zonal-mean, vertical warming pattern

a. *External CO_2 forcing*

The atmosphere and surface radiative heating from the external forcing alone ΔF^{ext} is examined by applying the linear decomposition in (1) to the radiative heating rate perturbations from the CO_2 forcing (Fig. 2). The zonal mean of the vertical distribution shows an arch shape of the maximum radiative perturbation with a peak value greater than $+1\,\mathrm{W\,m^{-2}}$ centered in the equatorial midtroposphere and extends poleward into the lower troposphere and to the surface. This ΔF^{ext} feature results from the meridional variation of atmospheric opacity to the longwave radiation associated with the latitudinal variation of the time-mean water vapor, as discussed in Cai and Tung (2012). The tropical surface and lower-tropospheric ΔF^{ext} is smaller because the resulting increase in the downward LW emission from increased CO_2 concentration is quickly absorbed by the water vapor (in the unperturbed time-mean state) before it reaches the layers below. Moving poleward, the water vapor concentration decreases rapidly and as a

result the maximum ΔF^{ext} occurs lower in the atmosphere as the latitude increases. This feature is reflected in the surface ΔF^{ext} (Fig. 2b; red line) by a minimum value at the equator that increases poleward. The surface value of ΔF^{ext} is larger over the Antarctic than the Arctic, which reflects the occurrence of more low-level clouds and moisture in the unperturbed climate-mean state of the Arctic, leading to the maximum absorption of the additional LW radiation in the Arctic atmosphere. Above the midtroposphere ΔF^{ext} maximum is a band of negative ΔF^{ext}. As shown in Cai and Tung (2012), an increase of CO_2 alone (without any feedbacks) causes an increase in downward radiation and a reduction in upward radiation in all atmospheric layers. The increase in downward radiation is strongest in the lower troposphere and at the surface, whereas the reduction in upward radiation is strongest in the upper troposphere (not shown here, which is similar to what is shown in Fig. 2 of Cai and Tung 2012). The sum of the convergence of the increase in downward radiation fluxes and the reduction in upward radiation fluxes corresponds to the profile of the increase in the net radiation heating due to the doubling of CO_2. In the elevations between the maximum increase in the downward radiation and the maximum reduction in downward radiation, the increase in downward radiation fluxes due to increased CO_2 concentration is divergent, and the reduction of upward radiation fluxes is convergent. It follows that these negative radiative heating perturbations in the troposphere result from a relatively large divergence of downward radiation fluxes and a small convergence of upward radiation fluxes, located between the maximum increase in the downward radiation and the maximum reduction in downward radiation. Above these negative heating layers, the convergence of the upward radiation fluxes is larger than the divergence of the downward radiation fluxes, responsible for the heating perturbation there. This explains the vertical band structure of the external forcing in the troposphere. The vertical elevation of the cooling perturbations is determined mainly by the elevation of the maximum increase in downward radiation, which in turn is determined by the climatological mean meridional and vertical profiles of atmospheric water vapor and clouds. This explains the meridional variation of the vertical band structure of the external forcing in the troposphere.

Partial temperature perturbations from the external forcing alone ΔT^{ext} exhibit a broad tropospheric and surface warming accompanied by strong stratospheric cooling (Figs. 2c,d). The largest ΔT^{ext} values, about $+1.5$ K, generally follow the arch shape pattern of the maximum ΔF^{ext}. The quantity ΔT^{ext} is positive throughout the troposphere, excluding the atmosphere above the South Pole despite the negative band of ΔF^{ext} in the midtroposphere. This feature occurs because the CFRAM analysis accounts for the thermal radiation effect of the temperature response due to energy perturbations at a specific layer on the temperature in the layers above and below. In the stratosphere, ΔF^{ext} is responsible for large negative ΔT^{ext} ranging from -1 to -10 K. The stratosphere is more sensitive to energy perturbations because of a much weaker stratospheric Planck feedback from colder stratospheric temperatures and lower emissivity. The Planck feedback magnitude is proportional to the control climate temperature where cooler temperatures result in a lesser Planck feedback, a direct result of the Stephan–Boltzmann law. This effect also further strengthens the effect of a poleward increasing profile of ΔF^{ext} at the surface (Fig. 2b), resulting in a stronger reduction in the equator-to-pole surface temperature gradient (Fig. 2d).

b. Water vapor feedback

The radiative energy perturbations due to water vapor changes $\Delta^{WV}(S - R)$ are positive and largest at the surface with a rapid poleward-decreasing pattern. In the atmosphere, $\Delta^{WV}(S - R)$ exhibits a banded structure in the vertical (Fig. 3a). The banded structure is more pronounced in the tropics and subtropics where $\Delta^{WV}(S - R)$ changes its sign several times with height. As with the increase in CO_2, an increase in water vapor also causes an increase in downward radiation fluxes and a reduction in upward fluxes throughout the entire atmospheric column. However, the increase in water vapor in a warmer climate is not uniform because the water vapor storage in the atmosphere is strongly dependent on the climatological vertical and meridional profiles of temperature. The increase in atmospheric water vapor is at its maximum in the lower troposphere in tropics, where the climatological temperature is much warmer and the increase in atmospheric water vapor decreases very rapidly with height and latitude away from the lower tropical troposphere; the water vapor changes in terms of percentage are of similar magnitude in the tropics and polar regions. Such maximum increasing in water vapor in the lower tropical troposphere and rapidly decreasing profile of the increase in water vapor away from the lower tropical troposphere yield two local maxima of the increase in downward radiation fluxes in the vertical over the tropics and subtropics (not shown here). However, the vertical profile of the reduction in upward radiation fluxes is not sensitive to such highly nonuniform increase of water vapor, exhibiting a maximum reduction in the upper troposphere in the tropics and subtropics (not shown; note that in the extratropics the reduction of upward radiation fluxes is less noticeable

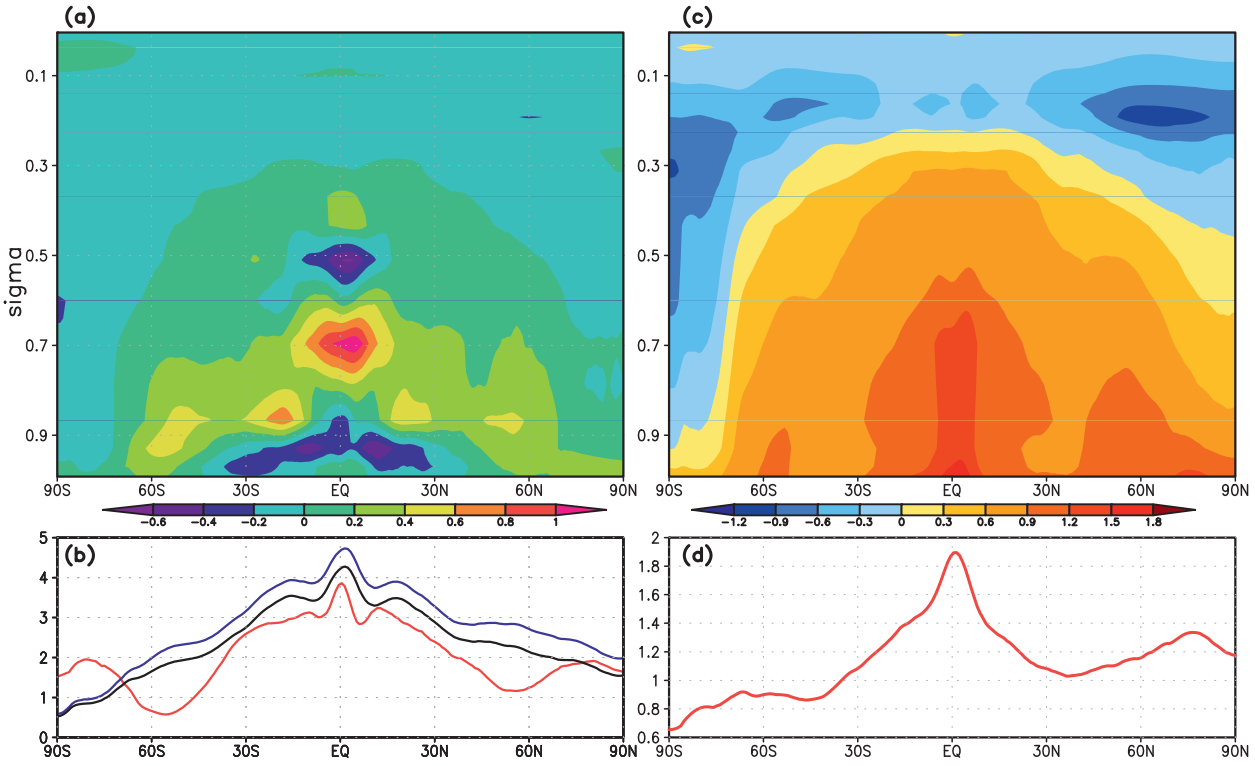

FIG. 3. As in Fig. 2, but for (a),(b) $\Delta^{WV}(S - R)$ and (c),(d) ΔT^{WV}.

because of the little change in water vapor there). Therefore, it is the vertical profile of the increase in downward radiation fluxes due to the vertically decreasing profile of the increase in water vapor that gives rise to the multiple band structure of $\Delta^{WV}(S - R)$ in the vertical in the tropics and subtropics. Note that the meridional profile of surface $\Delta^{WV}(S - R)$ is similar to its counterparts at the TOA and tropopause (Fig. 3b) and the latter aligns well with results from Community Climate System Model, version 3 (CCSM3; Taylor et al. 2011a). Based on this alone, one could state that most of the energy perturbation at the TOA due to water vapor feedback is applied to the surface. However, what takes place at the surface is due to the enhancement of the downward radiation from the lower troposphere where the water vapor change is greatest, whereas the net radiative energy flux perturbation at the TOA is due to the reduction of upward radiation energy fluxes caused by the increased upper-tropospheric water vapor. Therefore, it is mainly the strengthening of the downward LW radiation due to the moistening of the lower atmosphere that causes the warming in the lower troposphere and surface, whereas the reduction in upward LW radiation due to the moistening of the upper troposphere only contributes to the warming in the midtroposphere.

The minimum surface $\Delta^{WV}(S - R)$ is found near 60° in each hemisphere instead of at the poles, despite a larger specific humidity change at 60° than at the poles. Coinciding with this local minimum at the surface is a deep layer of positive $\Delta^{WV}(S - R)$ in the atmosphere, which is associated with a high concentration of liquid clouds in the lowest layers in the CCSM4 mean climate state (Fig. 4). The presence of these clouds in the lower troposphere absorbs extra downward radiative fluxes emitted from the moistened layers in response to the anthropogenic forcing causing a stronger and deeper $\Delta^{WV}(S - R)$ in the atmosphere and reducing the surface $\Delta^{WV}(S - R)$.

The partial temperature change pattern from the water vapor feedback ΔT^{WV} shows a decreasing pattern from the equatorial surface maximum of ~1.9 K in both vertical and meridional directions (Figs. 3c,d). At the surface, the water vapor feedback warms the equatorial region more than near the poles. The equatorial surface maximum of ΔT^{WV} decreases at different rates poleward depending on the hemisphere. In the Northern Hemisphere, ΔT^{WV} decreases to about +1 K at 40°N and then begins increasing until 80°N. In the Southern Hemisphere, ΔT^{WV} decreases to about +0.9 K at 40°S and remains at that value until 80°S where it begins dropping toward the pole due to the enhanced emission space. This feature results in a larger water vapor–induced equator-to-pole temperature gradient in the Southern Hemisphere. Atmospheric ΔT^{WV} is generally

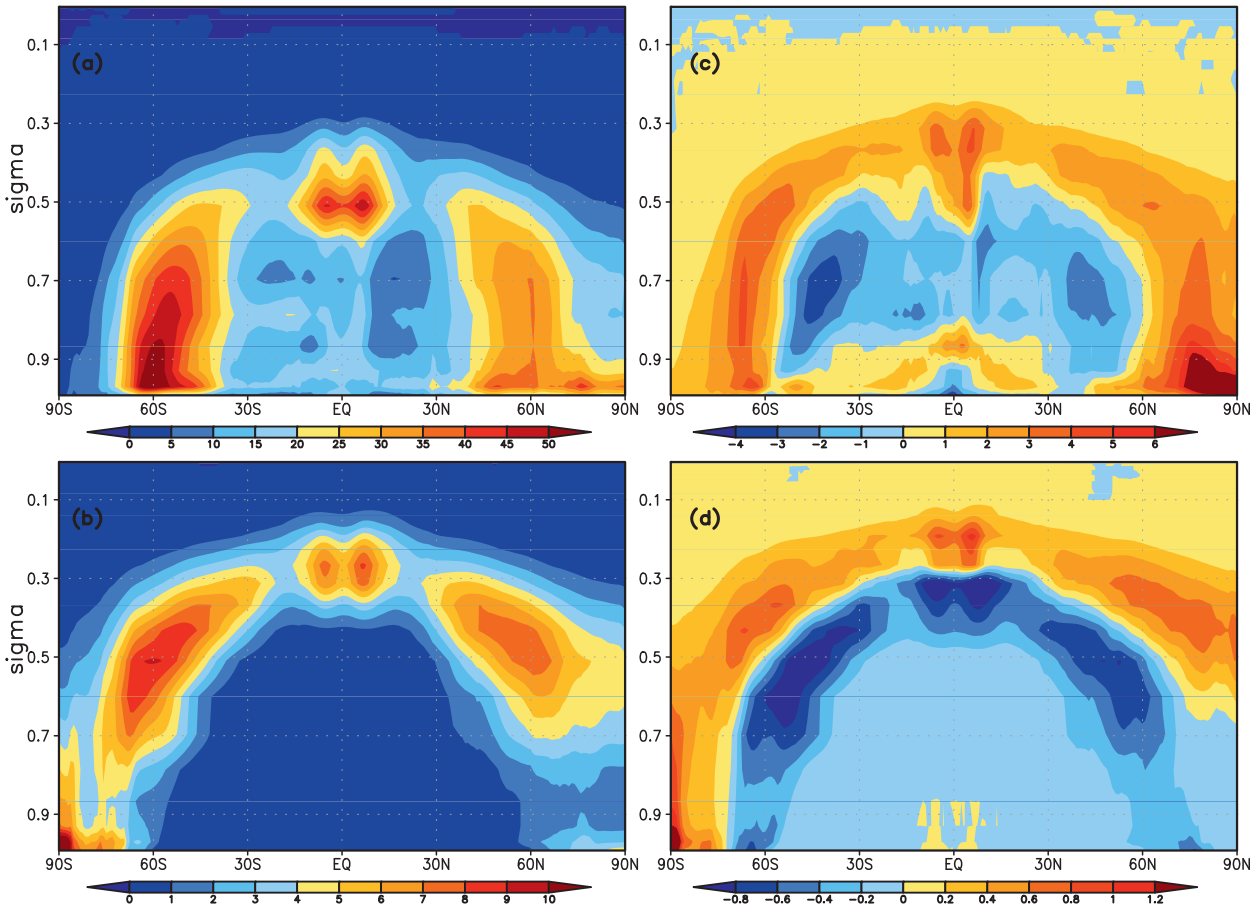

FIG. 4. Zonal-mean CCSM4 control climate mean cloud (a) liquid and (b) ice water mixing ratio, and cloud (c) liquid and (d) ice water mixing ratio response to CO_2 forcing (ppm by weight). Cloud fraction changes are not shown because over the regions where cloud liquid or ice water path increased (decreased), cloud fraction also increased (decreased). The exception is midlevel clouds in the tropics, which become thinner (less water content) with a larger fractional coverage.

positive in the troposphere, except over Antarctica where ΔF^{WV} is negative throughout the atmosphere above the boundary layer. A weak vertical variation of ΔT^{WV} is found in the tropics and subtropics despite the banded ΔF^{WV} structure due to the nonlocal temperature response to energy perturbation via thermal radiation coupling retained in CFRAM. Most of the nonlocal temperature response in the lower troposphere comes from the enhanced LW radiation due to the surface temperature warming forced by the surface ΔF^{WV}.

c. Cloud feedbacks

Cloud radiative energy perturbations are separated into longwave ($-\Delta^c R$; Fig. 5) and shortwave ($\Delta^c S$; Fig. 6) components. The offline computed cloud radiative heating rate perturbations are consistent with the CCSM4 responses in liquid and ice cloud concentrations (Figs. 4c,d) as well as the response in cloud fraction (not shown).The $-\Delta^c R$ (Figs. 5a,b) contains a rich meridional and vertical structure summarized by four characteristics: 1) equatorial banded structure in the vertical, 2) midlatitude low- and midtropospheric positive $-\Delta^c R$, 3) upper-tropospheric positive and negative belts of $-\Delta^c R$, and 4) LW cooling and heating of the polar troposphere and surface (Fig. 5c), respectively. The equatorial banded structure in the vertical results from the combined CCSM4 tropical mean state cloud distribution and the cloud response where the control climate trimodal cloud distribution shifts to a slightly higher level in the transient CO_2 forcing simulation. Layers with increased cloud fraction experience increased LW absorption of upward radiation from below that which is greater than the increase in its LW emission, resulting in a $-\Delta^c R > 0$, whereas layers with decreased cloud fraction exhibit a radiative cooling due to a reduced absorption. The stronger absorption of the downward LW radiation resulting from the increased low cloud fraction and water path causes negative $-\Delta^c R$ at the surface. The reduction

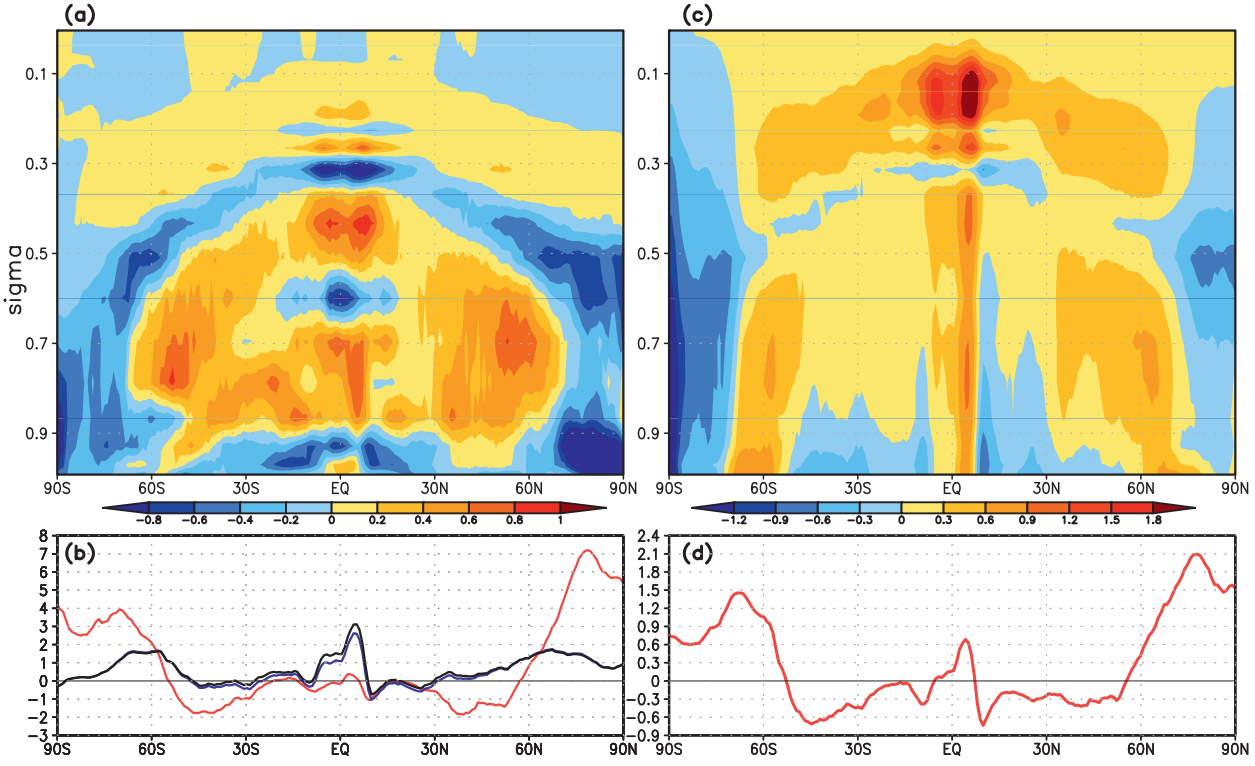

FIG. 5. As in Fig. 2, but for (a),(b) $-\Delta^c R$ and (c),(d) $\Delta T^{\text{cloud\_LW}}$.

in low- and midlevel water cloud fraction in midlatitudes causes a reduction of thermal radiation emission there, responsible for a strong positive $-\Delta^c R$ radiative heating perturbation. As indicated in Fig. 4, the arch shape of both liquid and ice cloud profiles extends both poleward and upward in response to the external forcing. Such a poleward and upward expansion in cloud distribution produces an arch shape of negative $-\Delta^c R$ in the place where clouds increase (due to a stronger emission) and another arch shape of positive $-\Delta^c R$ above due to a stronger absorption of the extra emission from below. The polar cloud response causes a cooling (heating) of the polar troposphere (surface). CCSM4 polar clouds are generally low and are composed of both water and ice. In response to the external forcing, these clouds show increases in cloud fraction and liquid water paths. Increased polar cloud fraction and optical depth drives a different $-\Delta^c R$ in the polar atmosphere than in the upper tropical troposphere. In the polar atmosphere, cooling rates are generated by the cloud fraction and optical depth increases because the layers are so dry that these cloud changes significantly increase layer LW emission. The increased polar atmospheric emissivity also increases the downward radiation from the atmosphere to the surface resulting in the maximum positive surface $-\Delta^c R$ (i.e., a stronger greenhouse effect).

Despite the complex structure of $-\Delta^c R$, the associated temperature perturbation $\Delta T^{\text{cloud\_LW}}$ vertical structure is quite smooth due to thermal radiative coupling built in the CFRAM analysis. The $\Delta T^{\text{cloud\_LW}}$ vertical structure is characterized by midlatitude and tropical atmospheric warming that is strongest in the upper tropical troposphere, a polar surface warming, and a cooling of the polar atmosphere. The LW cloud feedback contributes up to +1.5-K warming to the upper equatorial troposphere maximum (Fig. 5c), whereas cloud amount and liquid water path increases in the polar atmosphere cause significant cooling from about −0.5 to −1.5 K. At the northern and southern polar surface, the pronounced increase in downwelling radiation from the more cloudy atmosphere to the surface accounts for large surface $\Delta T^{\text{cloud\_LW}}$ up to +2.1 K.

Compared with $-\Delta^c R$, the SW perturbation of radiative flux convergence due to the cloud response ($\Delta^c S$) exhibits much weaker vertical structure because changes in $\Delta^c S$ are only involved with changes in absorption and reflection of solar energy but not emission. The $\Delta^c S$ is mainly confined to the surface because atmospheric absorption of SW radiation is weak and atmospheric $\Delta^c S$ is less than $-\Delta^c R$. As a result, almost all changes in $\Delta^c S$ at TOA represent the changes in $\Delta^c S$ at the surface, as indicated by the nearly exact overlapping of the black,

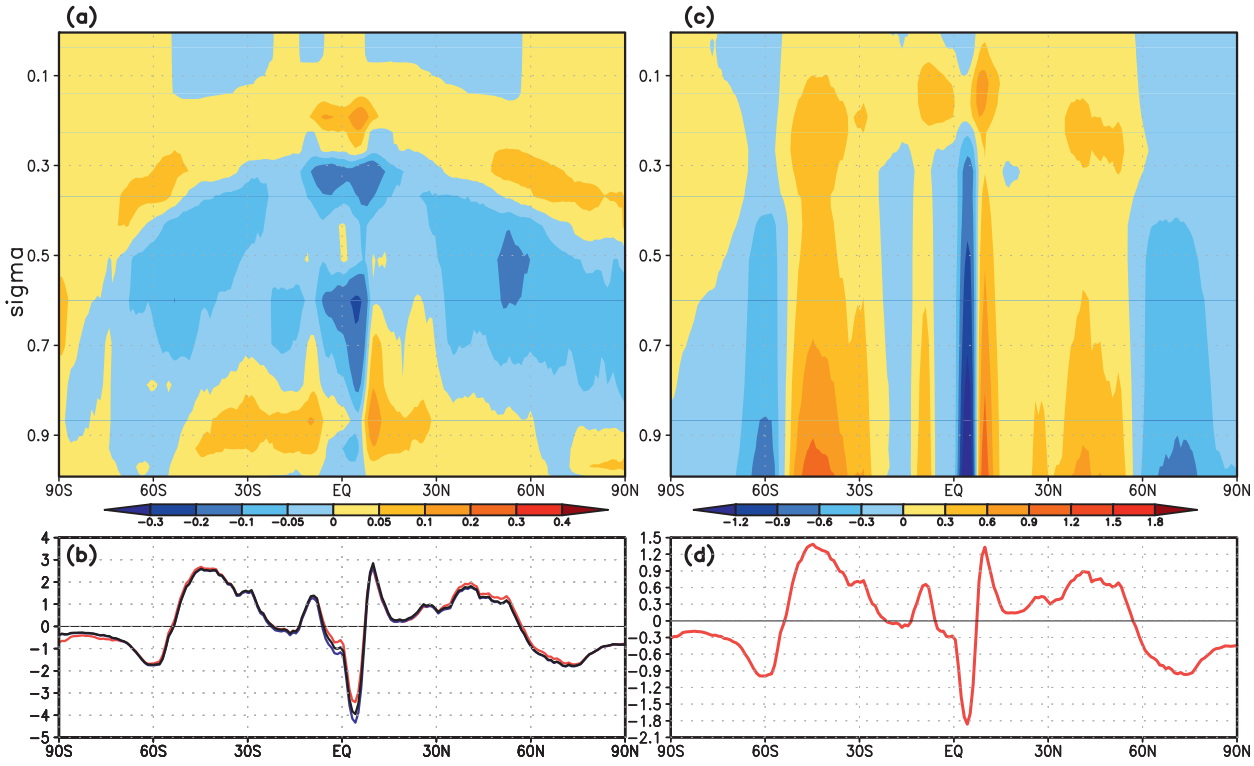

FIG. 6. As in Fig. 2, but for (a),(b) $\Delta^c S$ and (c),(d) $\Delta T^{\text{cloud\_SW}}$.

blue, and red curves shown in Fig. 6b. This is in sharp contrast to $-\Delta^c R$, which shows a large difference between the TOA and surface over the polar region. The surface $\Delta^c S$ meridional structure shows positive radiative perturbations in the subtropics and midlatitudes resulting from a decrease in the reflection of incoming solar energy by the thinning of lower and midtroposphere water clouds. Negative surface $\Delta^c S$ is found at the equator and in polar regions resulting from increased SW cloud reflection from the increased low cloud amount and optical depth. Small $\Delta^c S$ contributions within the atmosphere exhibit lower and upper troposphere positive perturbations and negative perturbations in the midtroposphere associated with enhanced (decreased) SW absorption where clouds increase (decrease) or become thicker (thinner).

Following $\Delta^c S$, large values of $\Delta T^{\text{cloud\_SW}}$ are mainly at the surface. Nevertheless $\Delta T^{\text{cloud\_SW}}$ is nonnegligible in the atmosphere due to the increased upward LW emission induced by $\Delta T^{\text{cloud\_SW}}$ at the surface. A strong $\Delta T^{\text{cloud\_SW}}$ value of about -2 K occurs just north of the equator adjacent to a significant surface warming of about $+1.2$ K. This feature driven by the coincident positive and negative surface $\Delta^c S$ caused by cloud liquid water path decreases and increases, respectively, suggests an intensification of the intertropical convergence zone that causes more reflection of the incoming solar energy by increased clouds there (Figs. 4c,d). This couplet of positive and negative cloud radiative perturbation largely offsets in the global mean. The strong positive surface $\Delta^c S$ in the subtropics and midlatitudes results in a strong surface warming. The $\Delta T^{\text{cloud\_SW}}$ in polar regions tends to slightly cool the surface and atmosphere.

Comparing the vertical and meridional structure of the net cloud radiative perturbations $\Delta^c(S - R)$ (Fig. 7a) with $-\Delta^c R$ (Fig. 5a) and $\Delta^c S$ (Fig. 6a) it is evident that the atmospheric structure of $\Delta^c(S - R)$ results from the LW cloud component, $-\Delta^c R$. At the surface, the strongest $\Delta T^{\text{cloud\_net}}$ is -1.2 K (Fig. 7d) centered near 5°N where $\Delta T^{\text{cloud\_SW}}$ dominates over $\Delta T^{\text{cloud\_LW}}$. Outside of this region, the $\Delta T^{\text{cloud\_net}}$ increases surface temperature. The $\Delta T^{\text{cloud\_net}}$ warms the upper tropical troposphere and cools the polar atmosphere (Fig. 7c) while warming the polar surface. Surface $\Delta T^{\text{cloud\_LW}}$ dominates over $\Delta T^{\text{cloud\_SW}}$ in the polar regions leading to an overall warming of the polar surface and a positive contribution to PWA (Figs. 5c,d; section 5). In summary, the main characteristics of the cloud-induced temperature response are that (i) clouds enhance polar surface warming via positive longwave feedbacks, (ii) clouds enhance upper-tropospheric warming especially in the

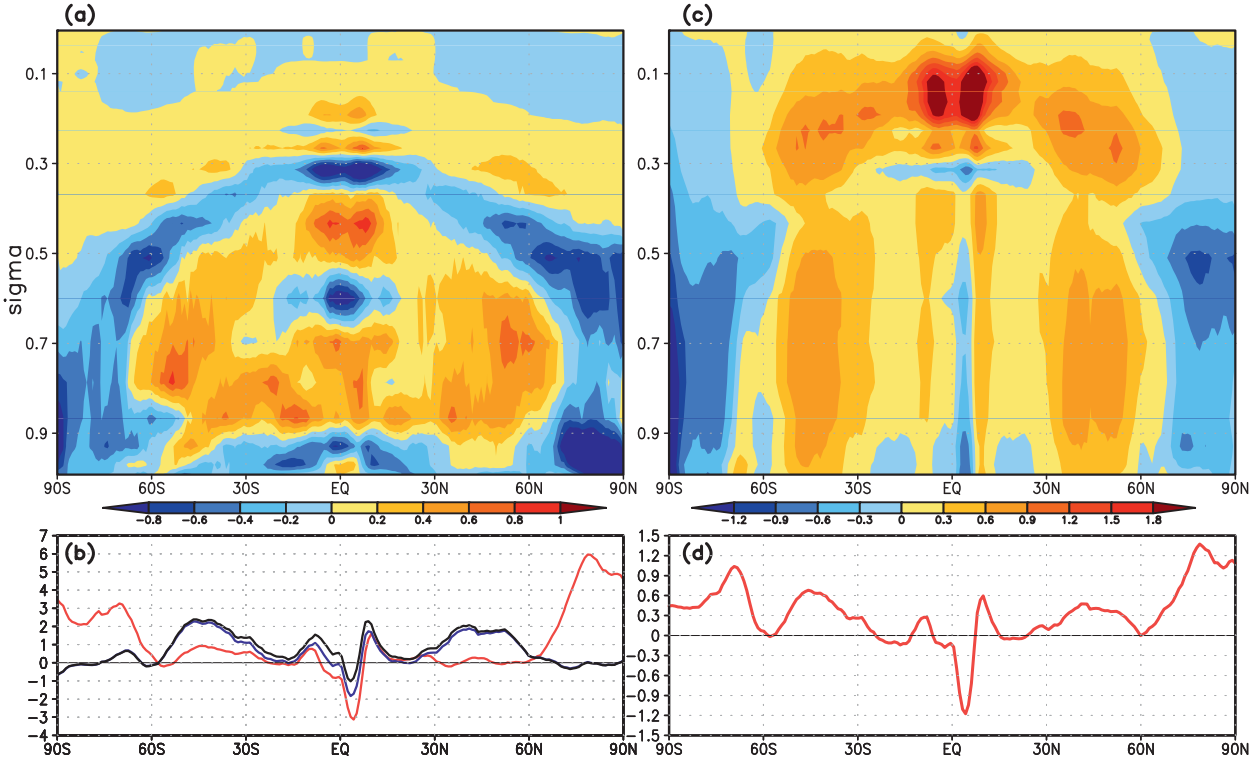

FIG. 7. As in Fig. 2, but for (a),(b) $\Delta^c(S - R)$ and (c),(d) ΔT^{cloud}.

tropics, (iii) LW cloud feedback mainly affects the atmosphere controlling the vertical distribution of the cloud-induced partial temperature perturbations, (iv) SW cloud feedback mainly affects the surface in the tropics and subtropics, and (v) the net effect of cloud feedback acts to generally reduce the equator-to-pole temperature gradient at the surface but enhances it in the upper troposphere.

d. Dynamical feedbacks

Changes in the energy transport, $\Delta Q^{\text{atmos\_dyn+storage}}$, are inferred from (3) and the atmospheric layer portion of the total radiative heating rate perturbations is shown in Fig. 8a, which includes both horizontal (total) energy transport through large-scale advection and vertical (total) energy transport through convection and large-scale vertical motions, as well as ΔQ^{LH} and ΔQ^{SH} whose vertical sums are equal to $-\Delta\text{LH}$ and $-\Delta\text{SH}$, respectively. The changes in vertical energy transport and ΔQ^{LH} dominate in the tropics, and the changes in horizontal energy transport and ΔQ^{SH} dominate in the extratropics. The tropical vertical structure of $\Delta Q^{\text{atmos\_dyn+storage}}$ exhibits a similar pattern to its counterpart in cloud property changes, showing negative in the lower and midtroposphere but positive in the upper troposphere. The pattern of negative values in lower levels and positive values in upper levels indicates the strengthening of tropical convection, which is accompanied by the increase in cloud-top height. The dominance of positive values of $\Delta Q^{\text{atmos\_dyn+storage}}$ in high latitudes or a poleward increase of $\Delta Q^{\text{atmos\_dyn+storage}}$ along the horizontal surface is indicative of a strengthening in poleward energy transport. This again is consistent with the poleward expansion of clouds shown in Fig. 4. The spatial variation of $\Delta Q^{\text{atmos\_dyn+storage}}$ inferred indirectly from the total radiative energy flux convergence perturbations is qualitatively similar to that directly evaluated from the dynamical core outputs of the same GCM model (Song et al. 2013), as well as similar to that of an idealized GCM model that does not include the hydrological cycle (Lu and Cai 2010; Cai and Tung 2012).

The partial temperature changes $\Delta T^{\text{atmos\_dyn+storage}}$ tend to enhance the warming in the upper tropical troposphere and at the surface over the polar areas (Figs. 8c,d). Figure 8c demonstrates that changes in atmospheric dynamical energy redistribution in response to anthropogenic forcing warms the upper tropical troposphere and the polar regions at the expense of the low and midtropical troposphere. Tropical upper-tropospheric $\Delta T^{\text{atmos\_dyn+storage}}$ exceeds +4.5 K in response to increased energy deposition likely from increased tropical convection. The $\Delta T^{\text{atmos\_dyn+storage}}$ (Fig. 8c) also

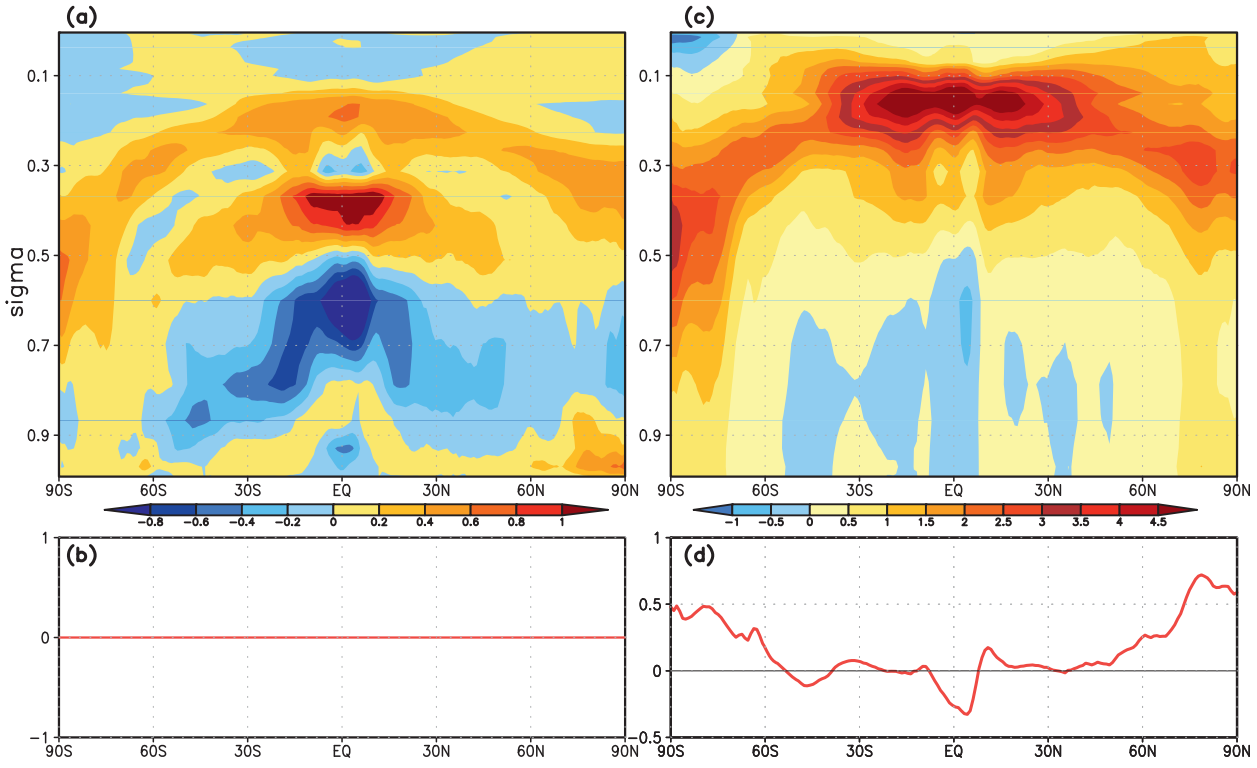

FIG. 8. As in Fig. 2, but for (a),(b) $\Delta Q^{\text{atmos\_dyn+storage}}$ and (c),(d) $\Delta T^{\text{atmos\_dyn}}$. The $\Delta Q^{\text{atmos\_dyn+storage}}$ is by definition zero at the surface.

shows significant contributions to Arctic and Antarctic upper-tropospheric warming and exceeds +2.5 K likely through increased poleward large-scale energy transport. A positive contribution by dynamic transport to polar amplification, $\Delta T^{\text{atmos\_dyn+storage}}$ with about +0.5 K, results from enhanced downward LW radiation to the surface in response to dynamical warming of the polar atmosphere despite surface $\Delta Q^{\text{atmos\_dyn+storage}} = 0$. The enhanced downward thermal radiation due to the dynamically induced atmospheric warming in high latitudes is the essential process that contributes to the dynamical amplification of the polar surface warming as elucidated first in Cai (2005) in a simple conceptual model and verified in Lu and Cai (2010) and Cai and Tung (2012) in a simple GCM.

e. Residuals

Figure 9 shows errors in the radiative heating rate $\Delta^{\text{Err}}(S - R)$ indicating errors in our offline radiative heating calculations with respect to the instantaneous CCSM4 simulated radiative heating rates and the corresponding partial temperature perturbation ΔT^{Err}. The largest values of $\Delta^{\text{Err}}(S - R)$ and ΔT^{Err} are found in several critical regions: upper troposphere, Arctic surface, and Antarctic atmosphere regions. The $\Delta^{\text{Err}}(S - R)$ in the upper tropical troposphere and in the atmosphere above Antarctica reach +1.5 W m^{-2} corresponding to ΔT^{Err} of +2 K over Antarctica and +1 K in the upper tropical troposphere. Significant negative ΔT^{Err} is shown in the upper tropical troposphere in the absence of a large local $\Delta^{\text{Err}}(S - R)$ resulting from large values of $\Delta^{\text{Err}}(S - R)$ in the column below, which reduces the LW radiation available for absorption at this level from that emitted below. The $\Delta^{\text{Err}}(S - R)$ reaches ±2.5 W m^{-2} at TOA, tropopause, and surface; however, surface ΔT^{Err} does not exceed ±0.8 K. Considering $\Delta^{\text{Err}}S$ and $-\Delta^{\text{Err}}R$ separately (not shown), atmospheric $\Delta^{\text{Err}}(S - R)$ is dominated by $-\Delta^{\text{Err}}R$, whereas $\Delta^{\text{Err}}S$ and $-\Delta^{\text{Err}}R$ show equal magnitudes at the surface. The $\Delta^{\text{Err}}(S - R)$ structure in the atmosphere resembles the $-\Delta^{c}R$ pattern suggesting that a major contribution to $-\Delta^{\text{Err}}R$ is from the LW cloud radiation calculation. The largest $\Delta^{\text{Err}}S$ is found mainly at the surface, as is the case with $\Delta^{c}S$, which suggests that $\Delta^{\text{Err}}S$ mainly comes from the SW component of the offline cloud radiation calculation. We also note that although $\Delta^{\text{Err}}(S - R)$ is very small in the stratosphere (less than 0.1 W m^{-2}), ΔT^{Err} can still be very large in the stratosphere because of the weaker Planck feedback in the stratosphere, resulting from a combination of less air mass and a relatively cool temperature in the stratosphere.

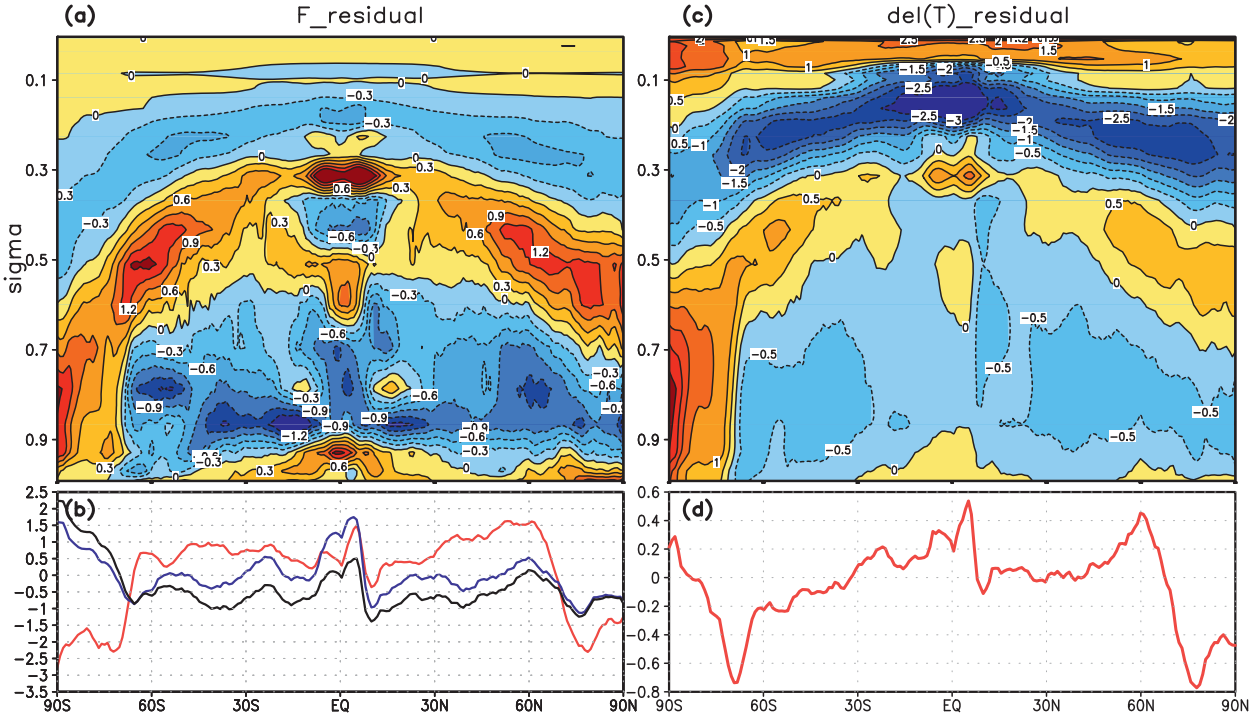

FIG. 9. As in Fig. 2, but for (a),(b) $\Delta^{\mathrm{Err}}(S - R)$ and (c),(d) ΔT^{Err}.

Residual errors are evident as all radiative feedback decomposition techniques and are quoted as being ~10% in magnitude (Soden and Held 2006; Soden et al. 2008). However, it is difficult to know exactly where these errors originate. It is generally speculated that these errors are due to the use of time-mean clouds in the offline radiative transfer calculation (Wetherald and Manabe 1988; Taylor et al. 2011a). Here, these errors are explicitly calculated so that the impacts can be known. The correlation noted between $\Delta^{\mathrm{Err}}(S - R)$ and $\Delta^{c}(S - R)$ indicates that clouds contribute largest to $\Delta^{\mathrm{Err}}(S - R)$, and the residual errors likely stem from differences between instantaneous and time-mean clouds (Kato et al. 2011). This result is applicable more broadly to all feedback decomposition techniques that use the time-mean clouds, instead of instantaneous clouds, in evaluating various feedback terms. Nevertheless, the apparent good negative correlation between $\Delta^{\mathrm{Err}}(S - R)$ and $\Delta^{c}(S - R)$ identified here may indicate that the cloud feedback evaluated using a time-mean cloud field, instead of instantaneous clouds, may just overestimate contributions to the total temperature changes by cloud feedback. This is specifically true in the upper tropical troposphere and at the tropical and polar surface. The impact of using the time-mean cloud field may have minimal impact on water vapor feedback and external forcing estimates, although it could have important impact on the surface albedo feedback over polar regions because $\Delta^{\mathrm{Err}}S$ and $\Delta^{\mathrm{alb}}S$ (which is evaluated using the time-mean clouds) also appear to be negatively correlated there.

f. Surface energy perturbations

The remaining contributions to the surface energy budget including surface albedo, turbulent heat fluxes, and ocean transport are shown in Fig. 10. The surface albedo change contributions are generally confined to extratropical and polar regions. Surface albedo radiative and partial temperature perturbations (Figs. 10a,b) extend equatorward farther in the Northern Hemisphere because 1) the model produces significant mountain snow and glacier melt in the Tibetan Plateau and 2) snow-covered land exists on the polar fringes in the control climate simulations. Southern Hemispheric surface albedo energy perturbations and partial temperature contributions are confined to the edges of the Antarctic continent. In these Southern Hemispheric regions energy perturbations exceed $3\,\mathrm{W\,m^{-2}}$ and account for about +3-K surface temperature warming. Surface and latent heat energy perturbations are also critical to the zonal-mean warming pattern of the Southern Ocean. In this region, ΔSH exceeds $-4\,\mathrm{W\,m^{-2}}$, whereas outside of the Southern Ocean ΔSH is generally positive and smaller than $\pm 2\,\mathrm{W\,m^{-2}}$. Physically, the

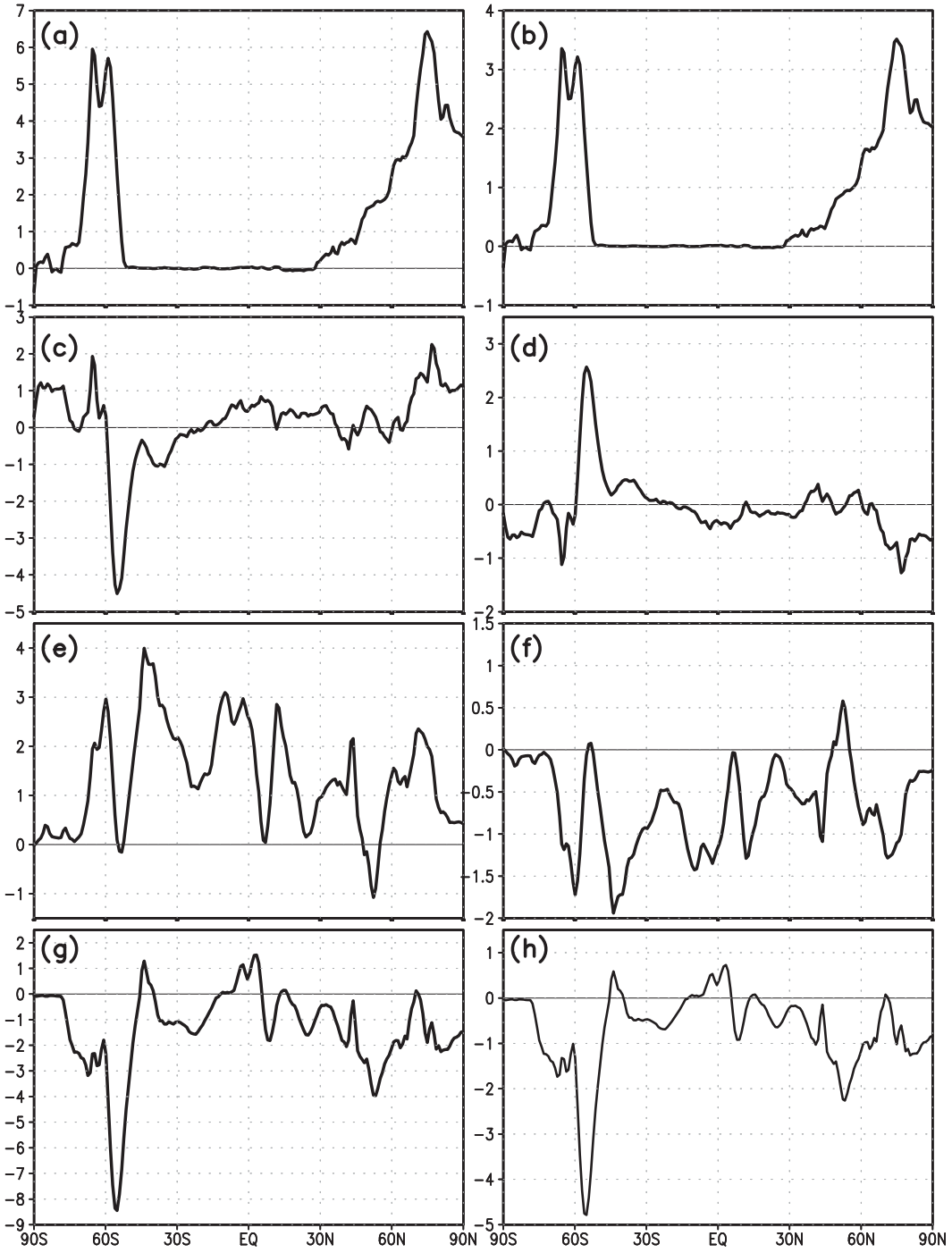

FIG. 10. (left) Energy perturbations at the surface and the (right) corresponding partial surface temperature changes: (a) $\Delta^{alb}S$, (b) ΔT^{alb}, (c) ΔQ^{SH}, (d) ΔT^{SH}, (e) ΔQ^{LH}, (f) ΔT^{LH}, (g) $\Delta Q^{ocn\_dyn+storage}$, and (h) $\Delta T^{ocn\_dyn+storage}$. The sign convection for the surface turbulent fluxes is positive from surface to atmosphere and therefore reductions in these fluxes warm the surface.

strength of turbulent sensible heat flux is controlled by the surface and near surface air temperature difference, as well as surface wind speed. This implies that the large negative ΔSH in the Southern Ocean occurs because the overlying atmosphere warms more than the surface. Southern Ocean ΔSH contributes to ΔT^{SH} of +2.5 K. In an opposing fashion, Southern Ocean ΔLH is markedly positive (Fig. 10e), $+3\ W\ m^{-2}$, tending to offset changes

in SH and corresponds to ΔT^{LH} of -1.5 K (Fig. 12f). Unlike ΔSH, ΔLH demonstrates significant contributions to changes in the surface energy budget zonal bands outside of the Southern Ocean, indicating that in several regions a significant negative evaporation feedback exists on the order of -1 K. The $\Delta Q^{ocn\_dyn+storage}$ represents both the spatial redistribution of energy by oceanic circulations and the ocean storage term. Positive values of $\Delta Q^{ocn\_dyn+storage}$ are mainly due to the convergence of the horizontal oceanic energy transport, whereas negative values are due to both the divergence of the horizontal oceanic energy transport and an increase in heat storage associated with downward mixing in the transient climate response. But the stronger negative values of $\Delta Q^{ocn\_dyn+storage}$ are mostly due to the heat storage. The global mean of $\Delta Q^{ocn\_dyn+storage}$ equals -1.16 W m^{-2}, which is entirely due to changes in the ocean heat storage term. This means that at the time of the doubling of CO_2, the ocean as a whole withholds about ¼ of the total radiative energy perturbation at the surface induced by the external forcing (0.72 W m^{-2}), water vapor feedback (2.27 W m^{-2}), albedo feedback (0.76 W m^{-2}), and cloud feedback (0.76 W m^{-2}). Such temporal withholding of energy flux at the ocean surface alone implies that at least another +0.6-K global warming is expected as the ocean reaches its own equilibrium (global mean of $\Delta T^{ocn\_dyn+storage} = -0.6$ K). According to Meehl et al. (2012), the global-mean equilibrium warming due to the doubling of CO_2 in CCSM4 coupled with a mixed-layer ocean model is 3.2 K. Therefore, the subsequent feedbacks in response to the final release of the temporal withholding of energy flux at the ocean surface contribute to another 0.96-K global-mean warming. The ratio of 0.96 to 0.6 K is about 1.6, which is nearly 3 times larger than the ratio of the global-mean temperature change due to all feedbacks at the time of the doubling of CO_2 (0.53 K = 1.64 K − 1.11 K) to the global-mean warming due to the doubling of CO_2 alone (1.11 K). This suggests that the feedback strength in response to the ocean heat storage is much stronger. Although we do not know the exact cause of this apparent change in climate sensitivity, the enhanced ocean heat storage in polar regions leads us to speculate that through additional melting of sea and land ice the polar regions play a critical role.

The largest $\Delta Q^{ocn\_dyn+storage}$ values occur in the Southern Ocean, indicating significant changes in ocean energy transport and energy storage that are responsible for a $\Delta T^{ocn\_dyn+storage}$ of between -4.8 and +5 K (Fig. 11). The area integral of negative $\Delta Q^{ocn\_dyn+storage}$ is far greater than the positive one, suggesting a significant portion of the surface energy perturbation in the Southern Ocean is stored in the deeper ocean layers and only a small portion of it is redistributed to the adjacent ocean columns. Significant $\Delta Q^{ocn\_dyn+storage}$ values are also found in the North Atlantic between 40° and 60°N (Fig. 11). Again, the area integral of negative $\Delta Q^{ocn\_dyn+storage}$ is far greater than the positive one, suggesting that the North Atlantic is another key location for the temporary storage of energy perturbations in the transient response phase of the global warming that postpones the warming at the time of the CO_2 doubling. The large ocean heat storage terms over the North Atlantic could be associated with the sinking branch of the deep thermocline circulation there, whereas the large ocean heat storage terms over the Southern Ocean could be due to stronger downwelling of heat associated with the speedy Antarctic Circumpolar Current.

5. Discussion: Process contributions to polar amplification

The northern and southern polar regions exhibit the strongest surface temperature responses (+3.76 and +2.58 K) and warming amplification factors with respect to global-mean warming of 2.3 and 1.6, respectively. From the CFRAM results, individual process contributions to the global, tropical (20°N–20°S), and polar region (60°–90°N and 60°–90°S) surface temperature changes are computed and shown in Fig. 12. Several differences between polar and tropical latitudes are evident. In tropical regions, only ΔF^{ext} and the water vapor feedback warm the surface; all other feedbacks are negative or very small (e.g., surface albedo feedback). In polar regions, longwave cloud, surface albedo, and atmospheric energy transports constitute positive feedbacks on surface temperature. The surface albedo feedback warms the northern and southern polar caps by 2.23 and 1.45 K, respectively. Removing the surface albedo feedback reduces the overall polar warming by 45%, which is enough to offset PWA. The net cloud feedback contributes +0.58 K to polar warming and results from the difference between two significant opposing LW and SW cloud feedback terms (+1.22 and −0.64 K averaged for both polar caps, respectively). Alternatively, tropical LW and SW cloud feedbacks are small and negative (−0.08 and −0.01 K, respectively). Removal of the net cloud feedback in polar regions reduces the total warming by 15% and 20% in the Northern and Southern Hemispheres, respectively. Polar warming by atmospheric heat transport and the external forcing are +0.37 and +1.40 K averaged over both polar caps, respectively. Ocean storage and heat transport and surface turbulent fluxes are the only cooling influences on the polar surface temperature response accounting for −0.93- and −1.13-K cooling average

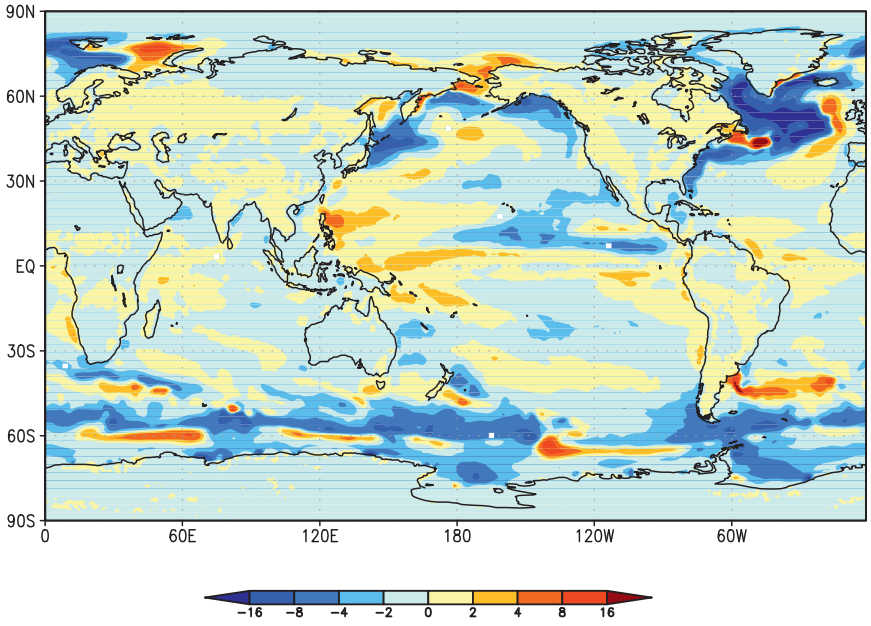

FIG. 11. Regional contributions of ocean heat transport and storage $\Delta T^{\text{ocn\_dyn+storage}}$ (K) to the transient surface temperature response.

over both polar caps. It is important to point out the above conclusion on the relative roles of surface albedo feedback versus cloud and dynamic feedbacks is made under the annual-mean condition. As reported in Lu and Cai (2009b) and Taylor et al. (2011b), the surface albedo feedback is dominant in the summer season, whereas cloud and dynamical feedbacks are dominant in the winter season when the polar surface warming is largest. We will report the contributions from the external forcing and individual feedbacks in giving rise to

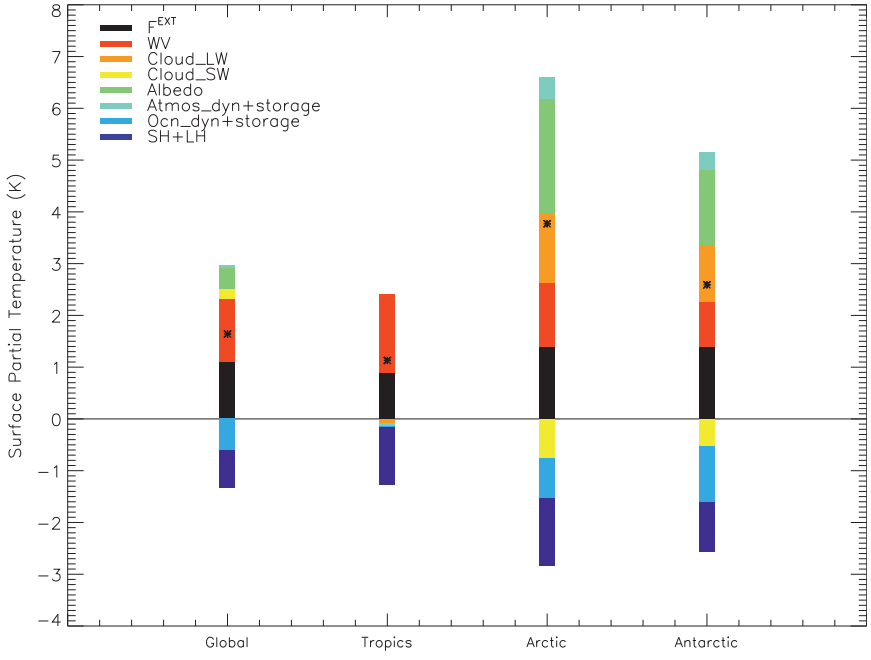

FIG. 12. Individual process contributions to the global, tropical (20°N–20°S), Arctic (60°–90°N), and Antarctic (60°–90°S) regional average surface temperature response. The black asterisk in each region denotes the sum of all partial temperature contributions.

TABLE 1. Individual process partial temperature contribution differences (K) in the Arctic (60°–90°N) and Antarctic (60°–90°S) regions with respect to global and tropical (20°S–20°N) mean contributions.

	Arctic − global	Arctic − tropics	Antarctic − global	Antarctic − tropics
ΔT^{ext}	0.28	0.50	0.29	0.51
ΔT^{WV}	0.04	−0.26	−0.35	−0.65
ΔT^{cloud_LW}	1.31	1.40	1.10	1.19
ΔT^{cloud_SW}	−0.94	−0.74	−0.72	−0.52
ΔT^{alb}	1.82	2.23	1.04	1.45
$\Delta T^{atmos\_dyn+storage}$	0.36	0.46	0.28	0.38
$\Delta T^{ocn\_dyn+storage}$	−0.17	−0.74	−0.48	−1.06
ΔT^{SH}	−0.48	−0.26	−0.38	−0.16
ΔT^{LH}	−0.10	0.06	0.16	−0.32
ΔT^{total}	2.12	2.64	0.94	1.46

the annual cycle of the spatial pattern in the CCSM4 global warming simulation in a separate paper.

Individual process contributions to the annual-mean PWA are quantified as the difference between the polar regions and the global or tropical mean surface temperature change (Table 1). This metric is used to quantify contributions to PWA to avoid normalizing by a small number. Surface albedo is the largest contributor to PWA in both hemispheres accounting for +1.82 K to Northern and +1.04 K to Southern Hemisphere PWA. Significant contributions to PWA are also made by the net cloud feedback, atmospheric heat transport, and the external forcing: +0.38, +0.32, and +0.29 K, respectively. The combined processes opposing polar amplification are similar magnitudes when averaging over both polar caps: ocean heat transport and storage, surface turbulent fluxes, and the water vapor feedback. However, hemispheric differences between these processes are significant. The cooling influence of ocean heat transport and storage is nearly 3 times larger in the Southern Hemisphere. Ocean heat storage and transport is much stronger over the North Atlantic Ocean than in the Southern Ocean but occurs over a much smaller area (Fig. 11). As a result, hemispheric ocean heat transport and storage differences are important contributors to the hemispheric PWA asymmetry in the CCSM4.

The present analysis indicates that the most important contributor to polar amplification is the surface albedo feedback, accounting for ~45% of the total polar warming, consistent with previous work (e.g., Hall 2004; Graversen and Wang 2009; Serreze et al. 2009). The positive contributions of atmospheric heat transport and the external forcing to PWA also agrees with previous results (e.g., Cai 2005; Lu and Cai 2010; Langen et al. 2012). However, Winton (2006) indicates that the external forcing opposes polar amplification, which is not supported by the present analysis. Winton (2006) drew this conclusion using a TOA energy budget perspective. The results show a much smaller contribution (10%) to the polar warming by atmospheric heat transport, which is consistent with Hwang et al. (2011), than Cai (2005; 25%) despite a similar magnitude of total PWA in the simple model. This difference with Cai (2005) is likely because clouds were not included in the simple model. This present study directly illustrates that clouds positively contribute to polar amplification by nearly equal amounts in both the Northern and Southern Hemispheres, consistent with some previous work (Holland and Bitz 2003; Lu and Cai 2009). However, this result opposes the inference from the traditional TOA or tropopause climate feedback framework (e.g., Soden et al. 2008). This difference is explained by considering column radiative heating rate perturbations by clouds (Fig. 7). The increase in polar low clouds increases the downwelling longwave radiation to the surface and at the same time enhances upwelling LW radiation from the atmosphere to TOA. The TOA perspective can only account for the slight increase in upwelling LW radiation from the atmospheric column and thus the SW cloud feedback effect dominates.

6. Summary and conclusions

This paper applies the CFRAM technique using offline radiative transfer calculations to isolate individual contributions from radiative and nonradiative feedback processes to the zonal-mean vertical temperature patterns in a transient 1% yr^{-1} CO_2 increase simulation of the NCAR CCSM4. The results indicate that the water vapor feedback and external forcing are the largest contributors to the global-mean surface temperature change, +1.21 and +1.11 K, respectively. Cloud feedback provides a weak positive contribution to global-mean surface temperature change, +0.20 K, mainly due to perturbations in absorbed surface SW radiation. From a global-mean perspective, the only negative contributions to surface temperature change are from

nonradiative feedbacks: surface evaporation feedback is −0.74 K and ocean heat transport and storage is −0.60 K.

In the atmosphere, the zonal-mean model temperature response is characterized by significant warming in the upper tropical troposphere and at the polar surface. Atmospheric warming by the external CO_2 forcing alone reaches +1.5 K and exhibits an arch shaped pattern where the apex is found in the midtropical troposphere. The feet are located at the high-latitude surface. The water vapor feedback contributes to a broad warming of the global troposphere and a cooling of the stratosphere; however, the largest warming of about +1.8 K is focused near the equatorial surface. The temperature response pattern from cloud feedback is complex with the largest warming of the upper tropical troposphere reaching +1.2 K. The majority of the troposphere is warmed by LW cloud feedbacks; however, a significant cloud-induced cooling is found in the polar regions. The net cloud feedback structure in the atmosphere results from LW cloud feedback, whereas at the surface LW and SW cloud feedbacks tend to contribute equally. Atmospheric energy transport is the largest contributor to tropical upper-tropospheric warming accounting for temperature perturbations larger than +3 K. Further, significant spatial correlation is indicated between cloud and atmospheric energy transport feedbacks suggesting a tight relationship between clouds and circulation changes.

Transient polar amplification at the time of CO_2 doubling is shown to be +2.12 and +0.94 K in the Northern and Southern Hemisphere, respectively, indicating polar amplification factors (ratio of polar to global-mean surface temperature change) of 2.3 and 1.6, respectively. These polar amplification factors are within the range of values given in Holland and Bitz (2003). The largest contributor to polar amplification is the surface albedo feedback, which contributes +1.82 and +1.04 K to polar amplification in the Northern and Southern Hemisphere, respectively. Contributions from the external forcing and atmospheric dynamic transport contribute secondarily to polar amplification. Ocean heat transport and storage, surface turbulent fluxes, and the water vapor feedback are found to oppose polar amplification. The results indicate several primary regions of ocean transport and heat storage, namely the Southern Ocean and the North Atlantic Ocean. Lastly, net cloud feedback is found to positively contribute to polar amplification accounting for +0.38-K amplification in both hemispheres. The cloud contribution to polar amplification is driven by the enhanced downwelling longwave radiation to the surface, resulting from an increase in polar low cloud fraction and liquid water path. Further, the increase in polar low clouds has been indicated to the most likely scenario for the polar clouds response to increases in CO_2 (Vavrus et al. 2009) and therefore clouds are most likely a positive contributor to PWA. The overall importance of clouds to PWA is likely to be somewhat model dependent. However, the features of the CCSM4 atmospheric and surface temperature response to a transient CO_2 forcing are consistent with expected features, including amplified warming of the tropical upper troposphere. Therefore, it is unlikely that general features of these results are very different in other models.

Globally, the ocean heat storage term is found to withhold ~25% of the total transient radiative forcing resulting from both CO_2 increase and climate feedbacks. This indicates that the globe will warm by at least another +0.6 K as the global-mean partial temperature perturbation from ocean heat storage is −0.6 K. The equilibrium response of CCSM4 to CO_2 doubling is quoted as +3.2 K using an ocean mixed-layer model, which indicates that to reach equilibrium feedback processes it must contribute another 0.96 K. Thus, the global-mean surface temperature appears to be 3 times more sensitive to the energy stored in the ocean than to the external CO_2 forcing itself. We speculate that the polar regions could play a critical role in this apparent time dependence of climate sensitivity due to the larger sensitivity of these regions and because significant portions of the global ocean heat storage occurs in polar regions.

Acknowledgments. This research was in part supported by research grants from the National Science Foundation (ATM-0833001 and ATM-0832915), the NOAA CPO/CPPA program (NA10OAR4310168), and DOE Office of Science Regional and Global Climate Modeling (RGCM) program (DE-SC0004974). Portions of this study were supported by the Office of Science (BER), U.S. Department of Energy, Cooperative Agreement DE-FC02-97ER62402, and the National Science Foundation.

REFERENCES

ACIA, 2005: *Arctic Climate Impacts Assessment.* Cambridge University Press, 1000 pp.

Alexeev, V. A., and C. H. Jackson, 2013: Polar amplification: Is atmospheric heat transport important? *Climate Dyn.,* **41,** 533–547, doi:10.1007/s00382-012-1601-z.

Barton, N. P., S. A. Klein, J. S. Boyle, and Y. Y. Zhang, 2012: Arctic synoptic regions: Comparing domain-wide Arctic cloud observations with CAM4 and CAM5 during similar dynamics. *J. Geophys. Res.,* **117,** D15205, doi:10.1029/2012JD017589.

Bitz, C. M., K. M. Shell, P. R. Gent, D. A. Bailey, G. Danabasoglu, K. C. Armour, M. M. Holland, and J. T. Kiehl, 2012: Climate

sensitivity of the Community Climate System Model, version 4. *J. Climate,* **25,** 3053–3070.

Bony, S., and Coauthors, 2006: How well do we understand and evaluate climate feedback processes. *J. Climate,* **19,** 3445–3482.

Cai, M., 2005: Dynamical amplification of polar warming. *Geophys. Res. Lett.,* **32,** L22710, doi:10.1029/2005GL024481.

——, 2006: Dynamical greenhouse-plus feedback and polar warming amplification. Part I: A dry radiative-transportive climate model. *Climate Dyn.,* **26,** 661–675.

——, and J.-H. Lu, 2007: Dynamical greenhouse-plus feedback and polar warming amplification. Part II: Meridional and vertical asymmetries of the global warming. *Climate Dyn.,* **29,** 375–391, doi:10.1007/s00382-007-0238-9.

——, and J. Lu, 2009: A new framework for isolating individual feedback processes in coupled general circulation climate models. Part II: Method demonstrations and comparisons. *Climate Dyn.,* **32,** 887–900, doi:10.1007/s00382-008-0424-4.

——, and K.-K. Tung, 2012: Robustness of dynamical feedbacks from radiative forcing: 2% solar versus 2 × CO_2 experiments in an idealized GCM. *J. Atmos. Sci.,* **69,** 2256–2271.

Chylek, P., C. K. Folland, G. Lesins, M. K. Dubey, and M.-Y. Wang, 2009: Arctic air temperature change amplification and the Atlantic multidecadal oscillation. *Geophys. Res. Lett.,* **36,** L14801, doi:10.1029/2009GL038777.

Fu, Q., and K. N. Liou, 1992: On the correlated *k*-distribution method for radiative transfer in nonhomogeneous atmosphere. *J. Atmos. Sci.,* **49,** 2139–2156.

——, and ——, 1993: Parameterization of the radiative properties of cirrus clouds. *J. Atmos. Sci.,* **50,** 2008–2025.

Gent, P., and Coauthors, 2011: The Community Climate System Model version 4. *J. Climate,* **24,** 4973–4991.

Gettelman, A., J. E. Kay, and K. M. Shell, 2012: The evolution of climate sensitivity and climate feedbacks in the Community Atmosphere Model. *J. Climate,* **25,** 1453–1469.

Graversen, R. G., and M. Wang, 2009: Polar amplification in a coupled climate model with locked albedo. *Climate Dyn.,* **33,** 629–643, doi:10.1007/s00382-009-0535-6.

Hall, A., 2004: The role of surface albedo feedback in climate. *J. Climate,* **17,** 1500–1568.

Hansen, J. E., A. Lacis, D. Rind, G. Russell, P. Stone, I. Fung, R. Ruedy, and J. Lerner, 1984: Climate sensitivity: Analysis of feedback mechanisms. *Climate Processes and Climate Sensitivity, Geophys. Monogr.,* Vol. 29, Amer. Geophys. Union, 130–163.

——, M. Sato, and R. Ruedy, 1997: Radiative forcing and climate response. *J. Geophys. Res.,* **102** (D6), 6831–6864.

Holland, M. M., and C. Bitz, 2003: Polar amplifications of climate change in coupled models. *Climate Dyn.,* **21,** 221–232.

Hwang, Y.-T., D. M. W. Frierson, and J. E. Kay, 2011: Coupling between Arctic feedbacks and changes in poleward energy transport. *Geophys. Res. Lett.,* **38,** L17704, doi:10.1029/2011GL048546.

Kato, S., and Coauthors, 2011: Detection of atmospheric changes in spatially and temporally averaged infrared spectra observed from space. *J. Climate,* **24,** 6392–6407.

Kay, J. E., and A. Gettelman, 2009: Cloud influence on and response to seasonal Arctic sea ice loss. *J. Geophys. Res.,* **114,** D18204, doi:10.1029/2009JD011773.

——, and Coauthors, 2012: Exposing global cloud biases in the Community Atmosphere Model (CAM) using satellite observations and their corresponding instrument simulators. *J. Climate,* **25,** 5190–5207.

Langen, P. L., R. G. Graversen, and T. Mauritsen, 2012: Separation of contributions from radiative feedbacks to polar amplification on an aquaplanet. *J. Climate,* **25,** 3010–3024.

Loeb, N. G., B. A. Wielicki, D. R. Doelling, G. L. Smith, D. F. Keyes, S. Kato, N. Manalo-Smith, and T. Wong, 2009: Toward optimal closure of the earth's top-of-atmosphere radiation budget. *J. Climate,* **22,** 748–766.

Lu, J., and M. Cai, 2009a: A new framework for isolating individual feedback processes in coupled general circulation climate models. Part I: Formulation. *Climate Dyn.,* **32,** 873–885, doi:10.1007/s00382-008-0425-3.

——, and ——, 2009b: Seasonality of polar surface warming amplification in climate simulations. *Geophys. Res. Lett.,* **36,** L16704, doi:10.1029/2009GL040133.

——, and ——, 2010: Quantifying contributions to polar warming amplification in an idealized coupled general circulation model. *Climate Dyn.,* **34,** 669–687, doi:10.1007/s00382-009-0673-x.

Manabe, S., and R. T. Wetherald, 1975: The effects of doubling the CO_2 concentration on the climate of a general circulation model. *J. Atmos. Sci.,* **32,** 3–15.

——, and R. J. Stouffer, 1980: Sensitivity of a global climate model to an increase in CO_2 concentration in the atmosphere. *J. Geophys. Res.,* **85** (C10), 5529–5554.

Medeiros, B., D. L. Williamson, C. Hanny, and J. G. Olson, 2012: Southeast Pacific stratocumulus in the Community Atmosphere Model. *J. Climate,* **25,** 6175–6192.

Meehl, G. A., and Coauthors, 2007: Global climate projections. *Climate Change 2007: The Physical Science Basis,* S. Solomon et al., Eds., Cambridge University Press, 747–846.

——, W. M. Washington, J. M. Arblaster, A. Hu, H. Teng, C. Tebaldi, W. G. Strand, and J. B. White III, 2012: Climate system response to external forcings and climate change projections in CCSM4. *J. Climate,* **25,** 3661–3683.

Pincus, R., H. W. Barker, and J.-J. Morcette, 2003: A fast, flexible, approximate technique for computing radiative transfer in inhomogeneous cloud fields. *J. Geophys. Res.,* **108,** 4376, doi:10.1029/2002JD003322.

Räisänen, P., H. W. Barker, M. F. Khairoutdinov, J. Li, and D. A. Randall, 2004: Stochastic generation of subgrid-scale cloudy columns for large-scale models. *Quart. J. Roy. Meteor. Soc.,* **130B,** 2047–2067.

Rind, D., 1987: The doubled CO_2 climate: Impact of the sea surface temperature gradient. *J. Atmos. Sci.,* **44,** 3235–3268.

——, R. Healy, C. Parkinson, and D. Martinson, 1995: The role of sea ice in 2 × CO_2 climate model sensitivity. Part I: The total influence of sea ice thickness and extent. *J. Climate,* **8,** 449–463.

Serreze, M. C., and R. G. Barry, 2011: Processes and impacts of Arctic amplification: A research synthesis. *Global Planet. Change,* **77,** 85–96, doi:10.1016/j.gloplacha.2011.03.004.

——, A. P. Barrett, J. C. Stroeve, D. M. Kindig, and M. M. Holland, 2009: The emergence of surface-based Arctic amplification. *Cryosphere,* **3,** 11–19.

Soden, B. J., and I. M. Held, 2006: An assessment of climate feedbacks in coupled ocean–atmosphere models. *J. Climate,* **19,** 3354–3360.

——, ——, and K. Shell, 2008: Quantifying climate feedbacks using radiative kernels. *J. Climate,* **21,** 3504–3520.

Solomon, S., and Coauthors, 2007: Technical summary. *Climate Change 2007: The Physical Science Basis,* S. Solomon et al., Eds., Cambridge University Press, 19–91.

Song, X., G. J. Zhang, and M. Cai, 2013: Quantifying contributions of climate feedbacks to tropospheric warming in the NCAR CCSM3.0. *Climate Dyn.,* doi:10.1007/s00382-013-1805-x, in press.

Taylor, P. C., R. G. Ellingson, and M. Cai, 2011a: Geographical distribution of climate feedbacks in the NCAR CCSM3.0. *J. Climate,* **24,** 2737–2753.

——, ——, and ——, 2011b: Seasonal contributions to climate feedbacks in the NCAR CCSM3.0. *J. Climate,* **24,** 3433–3444.

Vavrus, S., 2004: The impact of cloud feedbacks on Arctic climate under greenhouse forcing. *J. Climate,* **17,** 603–615.

——, D. Waliser, A. Schweiger, and J. Francis, 2009: Simulations of 20th and 21st century Arctic cloud amount in the global climate models assessed in the IPCC AR4. *Climate Dyn.,* **33,** 1099–1115.

Wetherald, R., and S. Manabe, 1988: Cloud feedback processes in a general circulation model. *J. Atmos. Sci.,* **45,** 1397–1415.

Winton, M., 2006: Amplified Arctic climate change: What does surface albedo feedback have to do with it? *Geophys. Res. Lett.,* **33,** L03701, doi:10.1029/2005GL025244.

Zelinka, M. D., and D. L. Hartmann, 2012: Climate feedbacks and their implications for poleward energy flux changes in a warming climate. *J. Climate,* **25,** 608–624.